# Effect of Spacer Length on Capturing Performance of Multivalent Aptamers Generated by Rolling Circle Amplification

**Zhong Wang**

Thesis submitted to the University of Ottawa

in partial fulfillment of the requirements for the

Master of Applied Science

Ottawa-Carleton Institute of Biomedical Engineering

Biomedical Engineering

University of Ottawa

## Abstract

Multivalent aptamer refers to a technique that joins two or more identical or different types of aptamer monomers together, with or without the presence of structural or other functional elements. As a rapid and easy method for fabricating the multivalent aptamer constructs, rolling circle amplification (RCA) has attracted great attention in recent decades. The incorporation of properly designed structural elements, such as intra-molecular spacers, have been shown to greatly enhance the efficiency of the multivalent aptamer system [1]. The objective of this current study is to systemically investigate the effect of different lengths of poly thymine spacer designs (polyT, from no spacer/NT, 5T, 10T, and 15T) on the capturing performance of RCA-generated multivalent system. To achieve this, we designed four circular probe templates by inserting zero, five, ten, and fifteen adenine bases (polyA). These polyA domains in the circular probe template are complementary to polyT with respective lengths in between the adjacent aptamers on the resultant RCA products (RCAPs). We found that the resultant RCAPs with length shorter than 10T showed a lack or low ability to capture target cells *E.Coli* O157:H7. When spacer lengths reach or exceed 10T, the capturing performance of the respective multivalent aptamer chain is significantly enhanced. This phenomenon can be explained by larger hydrodynamic sizes and less nonspecific secondary structures observed in RCAP with spacer length no less than 10T. Moreover, we found that there is also a trade-off that the number of polyA bases added into the circular probe template can significantly impair the efficiency of RCA reaction in respective to cyclization yield and amplification rate. The results of this research explain with details how the design of spacer affects RCA reaction efficiency and RCAPs' capturing performance, which provides ideas in designing an efficient RCA-generated multivalent system.

## Résumé

L'aptamère multivalent fait référence à l'assemblage de deux ou plusieurs monomères d'aptamère identiques ou différents, avec ou sans la présence d'éléments structuraux ou d'autres éléments fonctionnels. Étant une méthode rapide et facile pour fabriquer les constructions d'aptamères multivalents, l'amplification en cercle roulant (ACR) a attiré beaucoup d'attention au cours des dernières décennies. L'ajout d'éléments structuraux correctement modelés, tels que des espaceurs intra-moléculaires, peut grandement améliorer l'efficacité du système aptamère multivalent. Cependant, l'effet de la longueur de l'espaceur intra-moléculaire n'a pas encore été étudié dans un système d'aptamère multivalent généré par l'ACR. Cette étude a enquêté de manière systémique l'influence de l'insertion d'homo-oligonucléotides (poly thymine, polyT) de différentes longueurs (pas d'espaceur/NT, 5T, 10T et 15T) en tant qu'espaceur intramoléculaire dans un système d'aptamère multivalent généré par l'ACR. Nous avons conçu quatre modèles de sonde circulaire en insérant rien, cinq, dix et quinze bases d'adénine (polyA). Ces domaines polyA dans une matrice de sonde circulaire sont complémentaires de polyT avec des longueurs respectives dans les produits ACR résultants (PACRs). PACR avec des espaceurs intra-moléculaires plus courts que 10T a montré une incapabilité ou une faible capacité à capturer les cellules cibles *E.Coli* O157:H7. Lorsque la longueur de l'espaceur atteint ou dépassent 10T, la performance de capture de la chaîne d'aptamère multivalent respective sont considérablement améliorées. Ce phénomène peut s'expliquer par des tailles hydrodynamiques plus grandes et moins de structures secondaires non spécifique observée dans le PACR avec des espaceurs égaux ou supérieurs à 10T. De plus, nous avons constaté que l'insertion du polyA dans le modèle de sonde circulaire influençait de manière significative l'efficacité de la réaction ACR sous deux aspects, à savoir le rendement de cyclisation et l'efficacité d'amplification. Les résultats de cette recherche expliquent en détail comment la conception de l'entretoise affecte l'efficacité de la réaction ACR et les performances

de capture des PACR, ce qui fournit des idées pour la conception d'un système multivalent efficace généré par ACR.

## Statement of contribution

The entirety of this thesis was written by the author. All figures and tables were created by the author unless otherwise specified. The literature review section was edited by Nicholas Lee. The original idea of this study was inspired by Shuying Li. The work presented was largely performed by the author. The scientific guidance throughout the project and editorial comments for the written work were provided by Dr. Xudong Cao.

## Acknowledgements

I would like to thank my supervisor Dr. Xudong Cao for his consistent support and encouragement. I am grateful for the opportunities he has provided and his guidance throughout this project.

I would like to thank Dr. Jean-Philippe St-Pierre for his kindly support, for generously permitting me access to the experimental equipment in his lab. It would never be possible to finish this project without his support.

I would like to thank Shuying Li and Xingkai Hao for their patience and encouragement, for all of their help on this work, as well as the other members of our lab for being so kind and warm during my study.

Also, special thanks to Bo Zheng, Shuyun Wen, Nick De Luca, Danni Zou, Michael Sun, Lingruo Yang, and Jiajing Lin for their continuous support and encouragement during the progress of this project.

# Table of contents

# List of Figures

# List of Tables

## List of Abbreviations

| | |
|---|---|
| 2D | Two dimensional |
| 3D | Three dimensional |
| AuNP | Gold nanoparticles |
| ANOVA | Analysis of variance |
| APTES | (3-Aminopropyl) triethoxysilane |
| APS | Ammonium persulfate |
| C2C RCA | Circle-to-circle rolling circle amplification |
| cDNA | Complementary DNA |
| CTC | Circulating tumor cell |
| Cy3 | Cyanine 3 |
| DLS | Dynamic light scattering |
| DNA | Deoxyribonucleic acid |
| DNANT | DNA nanotube |
| dNTP | Deoxynucleotide |
| $ddH_2O$ | Double distilled water |
| D-RCA | Dumbbell probe-initiated rolling circle amplification |

| | |
|---|---|
| DTT | Dithiothreitol |
| dsDNA | Double-stranded deoxyribonucleic acid |
| dsRNA | Double-stranded ribonucleic acid |
| *E. Coli* | *Escherichia coli* |
| EDC | 1-ethyl-3-(3-dimethylaminopropyl) carbodiimide hydrochloride |
| EDTA | Ethylenediaminetetraacetic acid |
| E-RCA | Exponential rolling circle amplification |
| EtBr | Ethidium Bromide |
| Exo I | Exonuclease I |
| Exo III | Exonuclease III |
| FITC | Fluorescein isothiocyanate |
| HCR | hybridization chain reaction |
| HRCA | Hyper-branched rolling circle amplification |
| IDTE | 1× Tris/EDTA |
| LOD | Limit of detection |
| MANC | Multivalent aptamer nanoclimber |
| mbRCA | Multibranched rolling circle amplification |

| | |
|---|---|
| MES | 2-(4-morpholino)-ethane sulfonic acid |
| MIP | Molecularly imprinted polymers |
| NHS | N-Hydroxysuccinimide |
| PAGE | Polyacrylamide gel electrophoresis |
| PAMAM | Poly(amidoamine) |
| PBS | Phosphate buffered saline |
| PCR | Polymerase chain reaction |
| PDMS | Polydimethylsiloxane |
| PEG | Polyethylene glycol |
| PG-RCA | Primer-generated rolling circle amplification |
| polyA | Poly(adenine) |
| polyT | Poly(thymine) |
| RCA | Rolling circle amplification |
| RCAP | Rolling circle amplification product |
| RT | Room temperature |
| RNA | Ribonucleic acid |
| SELEX | Systematic evolution of ligands by exponential enrichment |

| | |
|---|---|
| siRNA | Small interfering RNA |
| sgRNA | Small guide RNA |
| SNP | single nucleotide polymorphisms |
| SSB protein | Single-stranded DNA binding protein |
| ssDNA | Single-stranded deoxyribonucleic acid |
| TBE | Tris/Borate/EDTA |
| TE | Tris/EDTA |
| TEMED | N,N,N’,N’,-tetramethylethylenediamine |

# Chapter 1. Introduction

Aptamers are short, single-stranded DNA or RNA molecules that bind to targets *via* specific structures [1]. Compared to antibodies, aptamers have advantages such as robust and large-scale production, small batch-to-batch difference, highly programmable structures, and longer shelf-life. However, not all aptamers have a desirable affinity toward their target. Taking advantages from multivalence effect, multivalent aptamer approaches can enhance the overall binding affinity (also known as avidity) of the aptamer construct. The avidity of multivalent aptamer constructs has been shown to be significantly enhanced with higher valency [2]. Among different methods for fabricating multivalent aptamer, rolling circle amplification (RCA) is one of the most used ways for generating surface-tethered aptamer chains. In an RCA reaction, a linear probe is cyclized to form a circular probe template—with a short oligonucleotide primer to generate a long single-stranded DNA—under the catalysis of specific polymerases (*e.g.,* phi29 DNA polymerase). The resultant RCA product (RCAP) contains hundreds to thousands of repeated aptamers that are covalently linked in a head-to-tail manner, with each repeating motif complementary to the circular probe template [3]. Based on the promising combination of multivalent aptamer and RCA, our group developed a multivalent aptamer-based fluorescent microfluidic sensor for detecting *E.Coli* O157:H7 using *in situ* RCA modified PDMS straight microfluidic channel. Our previous results showed that 3-fold more target cells were captured by the multivalent aptamer-modified channel compared with the aptamer monomer-modified channel [4].

Despite the advantages of this promising strategy, challenges still exist to be addressed: long DNA chains such as RCAP can induce inter- or intra-molecular interactions, thereby forming nonspecific double-stranded structures [5]. Moreover, the long DNA chains can collapse and intertwine into random micro-coils [6, 7], which reduces the accessibility of aptamer capturing regions [5, 8]. Xie et al. [9]

further clarified the relationship between aptamer-target interaction and the morphology of aptamer chains: after stretching the nonspecific structures in the aptamer chains by applying high temperature, significantly enhancement of cell enrichment efficiency was observed on two-dimensional PEG hydrogel (from 5.29% to 86%).

Here, we hypothesize that the above-mentioned nonspecific structures in multivalent aptamer chains can be separated and stretched by adding intra-molecular spacers with appropriate length between the adjacent aptamer capturing regions. Intra-molecular spacers refer to nonspecific elements in between the covalently linked aptamers. The incorporation of intra-molecular spacers has been shown to greatly enhance the efficiency of the multivalent aptamer for *in vivo* application [10]. Zhao et al. [8] also suggested that for RCA-generated multivalent aptamer chains to efficiently capture their targets, an intra-molecular spacer between aptamers was required. The spacers are generally made of polymers such as polyethylene glycol (PEG) or nonspecific DNA motifs (*e.g.*, poly thymine, polyT [11]), while polyT is the type with the deepest investigations due to its easiness of incorporation, net charge, and flexibility [12]. In an RCA-generated multivalent aptamer system, incorporating polyT spacers can be achieved by inserting the corresponding number of adenine bases into the circular probe template [11]. To the best of our knowledge, the optimal polyT spacer length to achieve maximum capturing efficiency and the mechanism behind this enhanced performance in an RCA-generated multivalent aptamer system has not been investigated yet.

The overall goal of this work is to systemically study the effect of polyT spacer length on the capturing performance of resultant RCAPs. Four linear probes with zero to fifteen adenine bases were designed for the *in situ* RCA modification of the microfluidic channel inner surface, using our previously established RCA-generated aptamer-modified PDMS microfluidic channel [4, 5]. The capturing performances of the RCAP were tested after running RCA for a pre-determined period. Our result demonstrated that the

RCAP with ten thymine bases spacers (i.e., 10T) shows the best capturing performance by extending the DNA chains outward from the dendrimer surfaces and reducing the level of nonspecific secondary structures. On the contrary, the corresponding longer linear probe can negatively affect the cyclization yield of the circular probe template and the amplification speed. Understanding how spacer insertion can affect the reaction efficiency and capturing performance of surface tethered RCAP has important meaning in designing other RCA-generated multivalent aptamer systems.

# Chapter 2. Literature Review

## 2.1. Multivalent Aptamer Structures

Based on their structures, multivalent aptamers can be briefly divided into three categories: spherical, single-layer, and linear, while the variety of other structures are also summarized in Section 2.4 (Figure 1). In general, aptamers of interest are composed of three parts: a headgroup moiety for attachment, a linker, and an outward-extending aptamer.

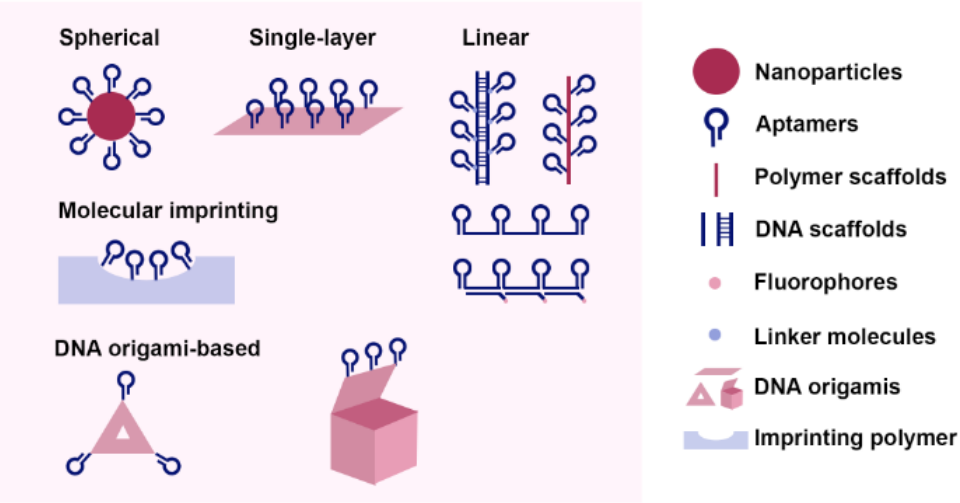


Figure 1. Schematic summary of the structures of multivalent aptamers.

### 2.1.1. Spherical multivalent aptamers

Spherical multivalent aptamers are a subtype of spherical nucleic acids. For spherical multivalent aptamers, the aptamers are connected onto a hollow or solid core particle by an organized, radial polyvalent arrangement [8]. The core particles can be gold [9], silver [10], metal oxides [11-13], silica [14, 15], polymers [16], or DNA self-assembly [17]. By taking advantage of the high loading capacity of these spherical particles, one can achieve much higher valency using these spherical multivalent aptamers in comparison with multivalent aptamers in other configurations. In addition, spherical carriers

also allow the greatest directional extension of aptamers into sample solutions, resulting in enhanced contact surface areas and thus better aptamer-target interactions. Furthermore, the plasmonic, catalytic, magnetic, or luminescent properties of the particles can also offer additional advantages for applications such as imaging and detection.

### 2.1.2. Single-layer multivalent aptamers

After the first ground-breaking study on the two-dimensional (2D) material graphene was published in 2004 [18], a new chapter has started in the history of material science. The atomic thickness of 2D materials is the origin of their unique physical and chemical properties, which are considerably different from those of three-dimensional (3D) structures. For example, their unique optical properties make them a promising tool for photothermal therapy [19], detection, and imaging applications [20]. Moreover, the large surface-to-volume ratio of 2D materials also allows for increased loading of therapeutic agents [21, 22]. Typical examples of 2D materials are graphene, transition metal dichalcogenides (e.g., molybdenum disulfide, $MoS_2$), and phosphorene.

Besides 2D materials, conjugating aptamers onto DNA origami nanosheets can also achieve single-layer aptamer configuration. This type of aptamer has been used as delivery vehicles for drugs [23, 24], antisense oligonucleotides [23], antimicrobial lysozymes [25], and RNase A [26]. Besides possessing high loading capacities and programmable structures, DNA origami-conjugated aptamers have also been shown to have good biocompatibilities. Additionally, the angstrom level precision of DNA origami scaffolds, and their excellent spatial addressability, make it possible to use them in the realization of single-molecule-level biosensing [27, 28].

### 2.1.3. Linear multivalent aptamers

Conjugating aptamers onto either flexible or rigid linear scaffolds allows aptamers to be arranged into linear configurations. The linear scaffolds can be made of polymers [29] or nucleic acids such as ssDNA [7, 30], dsDNA [31-33], DNA nanowires or nanotubes [34, 35]. The physical properties of each scaffold type confer specific advantages to their resultant linear constructs. For flexible scaffolds such as ssDNA and polymers, the scaffold chains can easily adapt to the surface topography of target cells while the multivalent aptamers work synergistically, thereby enhancing binding avidity [29]. Linear multivalent aptamers with flexible scaffolds are commonly used for therapeutic [1, 36] or detection purposes [7, 29, 37]. Because of these long and flexible aptamer chains, the linear multivalent aptamers can reach tens of micrometers into the sample solutions, thus providing sufficient contact opportunities with targets for more enhanced target captures [7]. In addition, these flexible multivalent aptamer chains have been shown to wrap around their targets, resulting in even higher target capturing efficacies [6]. In contrast, rigid scaffolds endow the aptamers with more precise arrangements and orientations. For rigid scaffolds, dsDNA, DNA nanowires, and nanotubes are the most commonly used scaffolding materials. These double-stranded nucleotide scaffold structures can also act as drug-loading sites for therapeutic agents [38, 39].

### 2.1.4. Other multivalent aptamer structures

Multivalent aptamer strategies can also be found in other configurations. For instance, in an attempt to increase the avidity of molecularly imprinted polymers (MIPs), multivalent aptamers have been used [40, 41]. After disassociation of template molecules, the polymers form binding sites and shapes complementary to the original template molecules. This MIP approach could find wider use in molecular recognition-based sensing and detection applications, especially if it is combined with multivalent aptamers to further enhance binding avidity [42, 43]. In addition, DNA origamis, such as

nanoboxes [44, 45], nanorobots [35], and tetrahedral [46, 47] or triangular origamis [48, 49], can also be used to construct nanostructures that feature multivalent aptamers, as shown in Figure 1.

### 2.2. Design strategies

The design of multivalent aptamer composites combines multiple identical or different aptamers with structural and other additional elements. The structural elements can be either a polymer (e.g., poly(ethylene glycol) (PEG)) or a non-specific nucleotide sequence (e.g., homo-polymeric oligonucleotides such as oligo-T with different lengths [7, 30, 36, 50]). These structural elements are designed to maintain intra- and inter-molecular space that allow for the independent activities of functional elements. Additional elements include nucleotide sequences such as DNAzyme, small interfering RNA (siRNA), or signaling probes. In order to achieve optimal performance, other factors in design are also considered, such as linkers, heterovalent aptamers, and spatial arrangement of the aptamers, as shown in Figure 2. These factors will be discussed individually in the following sections. By applying one or a combination of these strategies, the efficiency of multivalent aptamer composites can be further enhanced. For example, by combining linker designs with the usage of heterovalent aptamers, Lao and coworkers [51] demonstrated a hundred- to a thousand-fold enhancement of microarray sensitivity compared to single-type aptamers without any linkers.

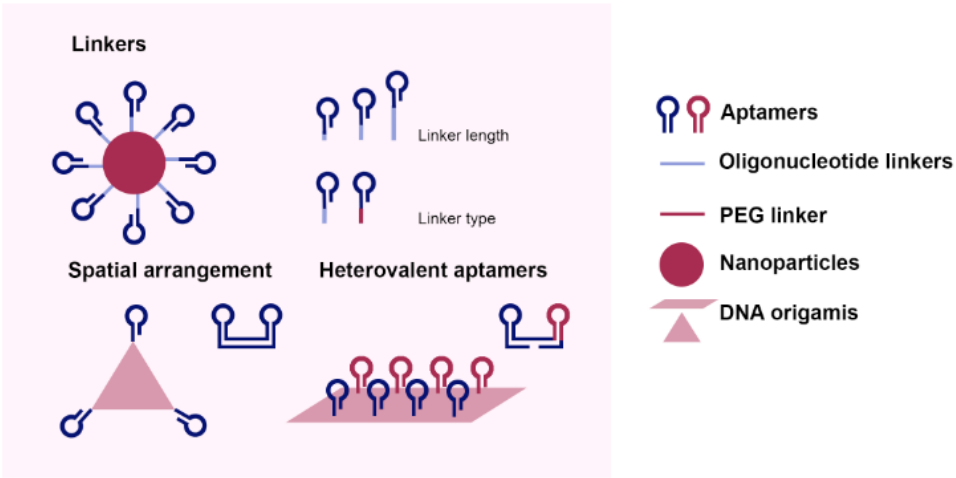

Figure 2. Schematic summary of designs that apply to multivalent aptamers. The optimization strategies include adding different lengths or types of linker motifs, using a mixture of two or more types of aptamers, and applying spatial arrangement of aptamers according to the geometry of target ligands or binding pockets.

### 2.2.1. Linkers

Linkers refer to short-strand polymers or oligonucleotides between the recognition domains of aptamers and the conjugated surface that they are attached to. Although multivalent aptamer strategies can enhance avidity compared to free aptamer monomers even without added structural elements [52], avidity can be further improved by employing properly designed linkers or spacers. This is because these linkers can either prevent adjacent aptamer units from interacting with each other to form unexpected secondary structures or offer enhanced abilities for surface tethered aptamers to properly bind to their targets.

In general, surface-tethered aptamers with linkers show better performance when compared with those without. With properly selected lengths and materials, linkers can increase the avidity of multivalent constructs by overcoming steric hindrances in adjacent aptamers. The most common linkers are PEG [53, 54], alkyl [54, 55], oligonucleotides such as oligo-T and oligo-A [54, 56, 57], and dsDNA [58]. Among different types of linkers, oligo-T linker is perhaps the most commonly used [51]; therefore, in this section, we will focus on discussing oligo-T linkers.

Linker length is an important consideration in linker design. Linkers with properly designed lengths should be able to support the aptamer sequence and allow the aptamers to stand out from the conjugated surface or backfilling molecules [59]. Surface-immobilized aptamers with relatively short linker lengths experience an impairment in freedom of Brownian motion [60], while relatively long linker lengths can be too long to ensure correct folding of either the aptamers [57] or the spacers themselves [61] for appropriate secondary structures. For instance, Qin and coworkers [57] demonstrated the importance of linker length by conjugating Sgc8 aptamers onto poly(amidoamine) (PAMAM) dendrimers *via* oligo-Ts with lengths of 5 to 20 nucleotides for circulating tumor cell (CTC) capturing. They found that excessively long linkers may lead to unfavorable alterations in aptamer secondary structures and thereby

limit the capture performance. In addition, Balamurugan and coworkers [62] further demonstrated the relationship between linker length and the affinity of surface-tethered aptamers using different linker lengths. As the length of the linker increased, a decreasing trend in aptamer surface density was observed. Similar results were also observed by Edwards and coworkers [63]. An increase in oligo-T spacer length resulted in decreasing number of aptamers immobilized onto the surfaces when compared with those without spacers. Furthermore, increasing electrostatic repulsion may also result in a charge barrier that inhibits the binding of additional aptamers to the surface [63].

### 2.2.2. Heterovalent aptamers

Heterovalent aptamer strategies, also known as aptamer cocktails, use two or more types of aptamers that target different moieties of the target. In comparison with using only one type of aptamer, heterovalent aptamer approaches have been shown to result in the cooperative enhancement of overall aptamer performances. For example, an 18-fold improvement of the limit of detection (LOD) was observed by using an aptamer cocktail-modified electrode (three different aptamers targeting different moieties on the surface of *E. Coli* cells) compared to an electrode modified with single-type aptamers [64].

The aptamer cocktail strategy also has shown potentials in CTC detections. Challenges for CTC detection include low CTC occurrence in clinical samples as well as targeting appropriate CTC surface ligands since presence of surface ligands on CTC surfaces is known to be non-uniform in-between individual patients [65]. This heterogeneity in target is particularly challenging: some well-studied ligands on CTC cells can have different expression levels between patients [66], thereby leading to inconsistent sensitivities. To overcome these obstacles, one can target various motifs to increase avidity and prevent the off-target effect due to the decrease or loss of certain biomarkers [67]. Lin et al. [65] developed a dual-aptamer-tethered network system that allowed DNA-triggered reversible isolation and

release of CTCs by tethering Sgc8c and Sgc4f aptamers onto a ssDNA scaffold. This dual-type aptamer network system showed significantly higher capturing efficiency compared to a single-type aptamer network. Zhao et al. [68] demonstrated a combined approach by combining aptamer cocktail strategy and microfluidic platform to detect CTCs, as shown in Figure 3. The researchers deployed a two-step *in vitro* selection of aptamer cocktails without previous knowledge of the binding motif and compared its effects with single-type aptamers; the selected aptamer cocktail showed a synergetic effect, resulting in higher overall capturing efficiency compared to the single-type aptamers.

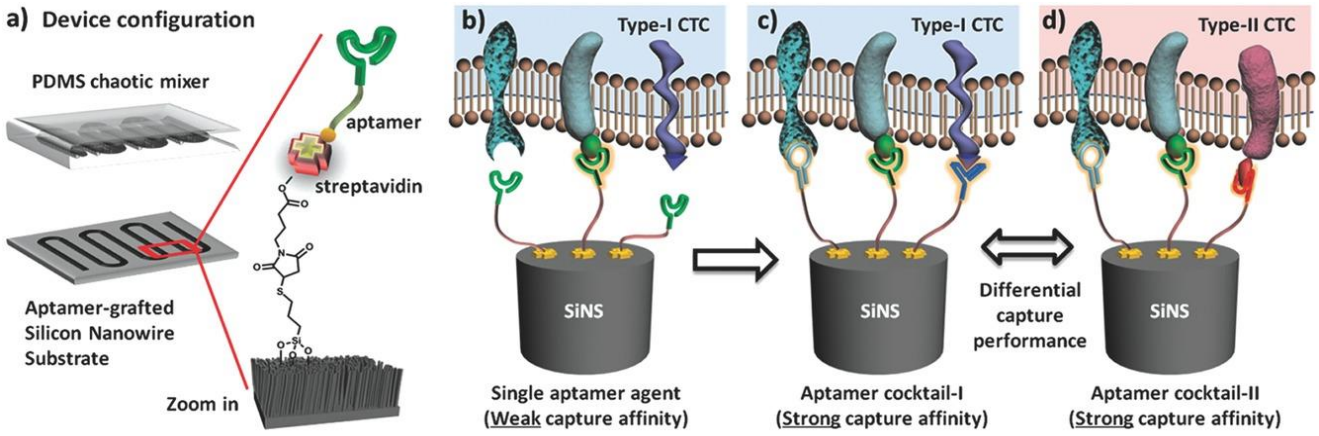


Figure 3.Schematic description of aptamer cocktail-based CTC microfluidic approach. a) A microfluidic device is composed of an aptamer-conjugated silicon nanowire and a PDMS chaotic mixer. b) When a single aptamer capture agent is incorporated, the capturing affinity of the device is relatively weak due to the lack of synergistic binding. c) By using an aptamer cocktail, the synergistic effects among individual aptamers lead to an enhanced capturing affinity. d) Different aptamer cocktails are expected to have differential capture performance for CTC subpopulation recognition (ref. 68).

Another way of utilizing heterovalent aptamers is multiplex testing, which enables the simultaneous testing of more than one target. Multiplex testing allows for significant savings in samples, reagents, and time used, thereby having crucial applications in situations such as point-of-care testing. By combining aptamer-conjugated gold nanoparticles (AuNPs) with magnetic graphene nanosheets, Dou and coworkers [69] developed a sensitive electrochemical platform for detecting CTCs in blood samples. Sgc8 and Td05 aptamers were both incorporated for targeting two types of CTCs: CCRF-CEM cells and

Ramos cells, respectively. This platform demonstrated successful detection of rare CTCs in clinical blood samples. In another interesting study, Dai et al. [70] developed an optical multiplex testing system based on a 3D triangular-shaped DNA nanotube (DNANT), as shown in Figure 4. As a proof-of-concept, three aptamers for targeting thrombin, ATP, and insulin were conjugated onto three edges of the nanotube. This work demonstrated the multiplex recognition capability of the aptamer-functionalized DNA nanotube: the aptamer-conjugated DNA nanotube can achieve multiple binding activities that also generate discriminative signals for multiple targets in a single system. The authors suggested that by simply altering the design of the scaffold from triangular to square, pentagonal, and hexagonal nanotubes, it is possible to simultaneously detect four, five, or even six targets.

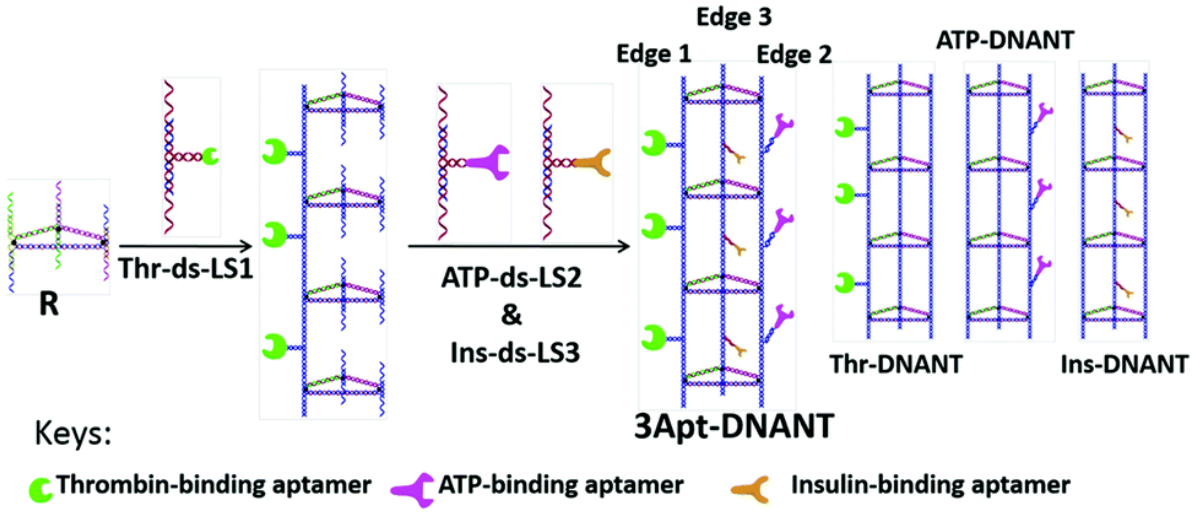


Figure 4.The schematic description of construction of 3 aptamer-DNANTs and schematic representation of thrombin-DNANT, ATP-DNANT and insulin-DNANT (ref. 70).

### 2.2.3. Spatial arrangement

The spatial arrangement of aptamers, or their positioning relative to binding motif alignments on the target surface, has become an exciting field in the study of multivalent aptamers. The optimal arrangement of aptamers—according to the distance and geometry of surface ligands or binding

pockets—is believed to be more important than high local concentration [1, 71] since placing aptamers at an optimal distance and position can result in increased avidity [72].

Spatial arrangement can be achieved by either altering the distance between two adjacent aptamers [73, 74] or positioning aptamers in a desired geometry [71, 75]. Distance arrangements can be achieved by positioning aptamers onto rigid scaffolds (*i.e.*, dsDNA, dsRNA [76], or DNA origami [77]). By conjugating two different anti-thrombin aptamers onto multi-helix DNA tiles and DNA origami scaffolds at various distances, Ke et al. demonstrated that placing two different thrombin binding aptamers at an optimal distance on a rigid DNA tile nanostructure could lead to significant improvements in binding affinity, with their results indicating an estimated fifty-fold enhancement in binding affinity compared to aptamer monomer approach [78]. Using rigid scaffolds for spatial arrangement is particularly effective when the arrangements of binding moieties on the target surface can be perfectly aligned with those of the aptamers. However, it should also be noted that even minor structural mismatches could lead to impaired binding due to unfavourable steric interactions in such cases [79].

Rigid DNA scaffold is also a powerful method for studying the geometric arrangement of aptamers, owing to its ability of positioning aptamers in very precise locations. By applying geometric positioning optimization and flexibility, Kwon et al. [71] developed a star-shaped multivalent aptamer-conjugated DNA architecture using tile-based DNA assembly based on the specific 2D arrangement of envelope protein domain III. In this star-shaped DNA nanoconstruct, each dsDNA intra-molecular spacer contains a hairpin structure, which can be unzipped, stretched, and fine tuned to fit the distance between adjacent surface ligands. This spatial arrangement of multivalent aptamers enhanced specific binding while reducing off-target binding through pattern identity. In contrast, linear aptamer complexes led to weaker affinity. One interesting aspect of this study was that the aptamers with a mismatched geometric

arrangement displayed an even lower affinity than the linear complex. As shown in Figure 5, a heptagon-shaped complex instead of a pentagon sterically prevents other complexes from binding despite correct spacing and a higher level of valency, strongly suggesting the importance of 2D geometric positioning [71].

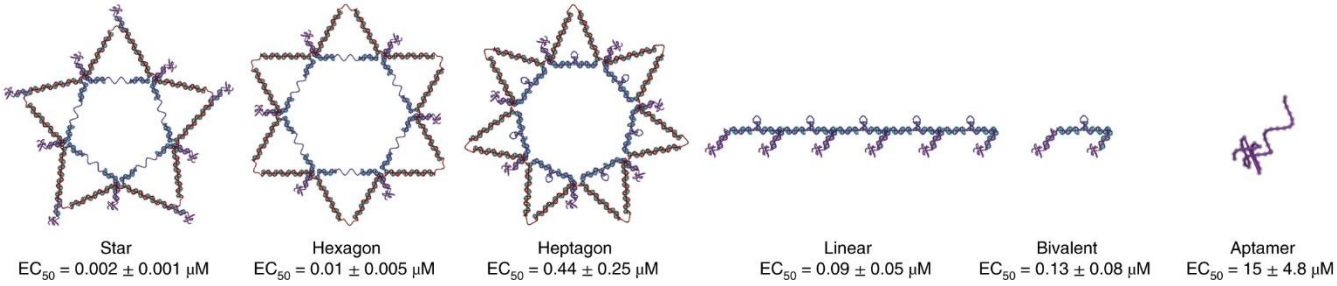


Figure 5. A schematic representing the inhibitory nanostructures for dengue virus with their corresponding mean EC50 (half maximal effective concentration) values. The hexagonal spacing resulted in reduced detection compared to the star-shaped spacing despite it being the correct spacing in theory. The schematic for the star and hexagon shows an unzipped hairpin region because potent pattern matching occurs. Other scaffolds represent the hairpins as stem-loop structures to indicate a lack of potent pattern matching (ref.71).

## 2.3. Biomedical and analytical applications

### 2.3.1. Biosensors

Aptamers are important recognition mechanisms in biosensing applications. In particular, multivalent aptamers allow elevated local concentrations of aptamers, increased binding avidity between the capturing motif and the target, and the increased nuclease resistance. As a result, the multivalent strategy has been widely used in many large-sized target detections, such as human cells [43, 65, 80-82] and bacterial cells [64, 83-85] assays, due to its increased binding avidity. In addition, the multivalent strategy has also been used to detect smaller sized targets, such as extracellular vehicles [30, 86] and small molecules [87]. In comparison with antibodies, aptamers allow readily and reversible release of their targets for further analysis and characterizations [88] due to externally applied factors such as complementary DNA strands [65, 89], restriction enzymes [6], temperature [88], or light [90].

Linear aptamers and spherical aptamers (see Figure 1) are the most frequently used aptamer forms in detection applications; to further increase multivalency, the combinations of the two forms have also been reported [83]. For instance, Chen et al. [13] presented a NanoOctopus to capture CTCs in blood samples. To achieve this, the researchers conjugated multivalent aptamer chains onto the surfaces of magnetic nanoparticles (i.e., NanoOctopus), and they showed that the multivalent NanoOctopus demonstrated significantly increased avidity to their targets. Similarly, DNA nanochains that contain multiple copies of aptamers are also used [6, 7, 83]. Inspired by climbing plants, Liu et al. [29] developed a multivalent aptamer nanoclimber (MANC)-functionalized PDMS microfluidic device for minimal residual disease testing, as shown in Figure 6. This work demonstrated a 57.5-fold increase in binding affinity when the MANCs was used to capture target cells in human plasma samples than mono-aptamer approach, suggesting that the MANCs incorporating multivalent aptamers are clinically applicable to assay minimal residual disease in the peripheral blood.

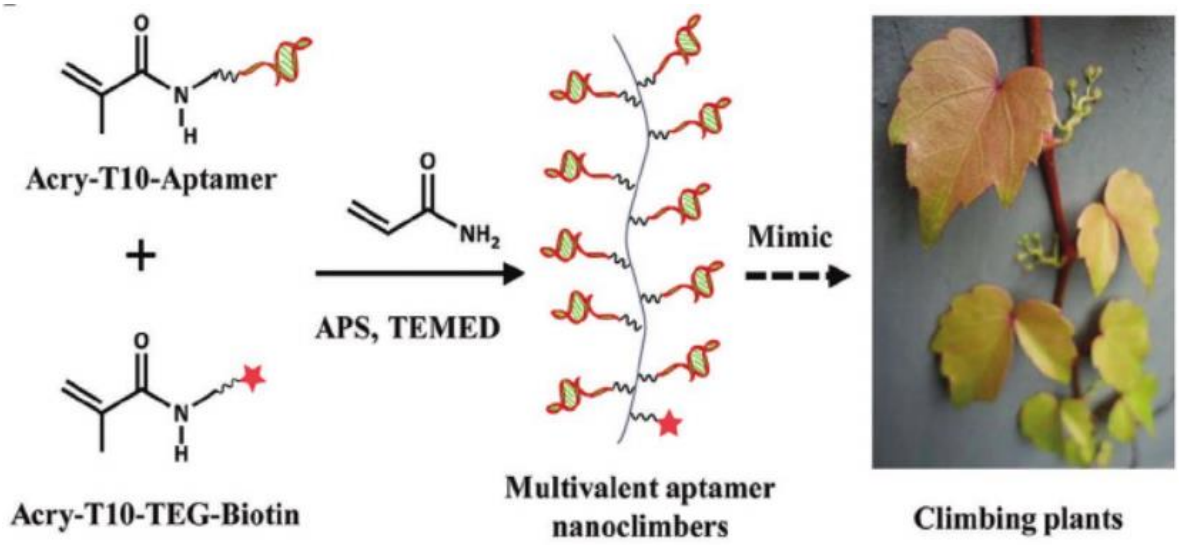


Figure 6.A schematic diagram of the synthetic process of MANC. In brief, under the catalysis of ammonium persulfate (APS) and N,N,N',N',-tetramethylethylenediamine (TEMED), acrylamide co-polymerizes with acrydite-T10-aptamer and acrydite-T10-TEG-Biotin to for a climbing plants-inspired multivalent structure (ref. 29).

Spherical multivalent aptamers have also been used in microfluidic devices [37, 82, 91, 92] to increase detection performance. Inspired by octopus tentacles, Song et al. [37] conjugated SYL3C aptamers onto AuNPs, which were then attached to the inner surfaces of a micropillar-decorated microfluidic channel. The researchers showed that this approach allowed approximately 250 SYL3C aptamers to be attached onto each AuNP and that the detection platform was able to detect CTCs directly in blood samples without any sample pre-treatment. In addition, the authors further demonstrated that the multivalent aptamer approach improved the binding efficiency by 100-fold and that the capturing efficiency was enhanced by more than 300% in blood samples when compared with aptamer monomer modified microfluidic devices. Alternately, polymeric dendrimers, such as PAMAM, have also been used to construct spherical multivalent aptamers structures [84]. Jiang and coworkers [83] developed a microfluidic platform for detecting *E. Coli* O157:H7 using RCA chain-conjugated PAMAM dendrimers as an inner-channel surface modification. In this work, the straight PDMS microfluidic channel was modified with PAMAM dendrimers conjugated with capturing long ssDNA chains containing hundreds of repeated aptamer units. The resultant channel modified by multivalent aptamer chains captured approximately 3-fold more target cells compared to a channel modified by aptamer monomers. Furthermore, this multivalency-driven improvement was observed to be more significant under higher flow rates, which suggested that this multivalent strategy can be a potential solution for achieving higher throughput in microfluidic devices. Additionally, PAMAM dendrimers have excellent antifouling properties that significantly reduce non-specific fouling and enhance the signal-to-noise ratio [93].

### 2.3.2. *In vivo* applications

Precisely delivering treatment vehicles requires specific processes between cell surface biomarkers and recognition elements [94]. This specific recognition process enables accumulation of therapeutic agents in pathological sites while reducing systemic toxicity [38]. Aptamer-mediated drug delivery systems can

take advantage of the enhanced avidity to their targets due to multimerization. Besides, DNA nanoparticles also enable the effective encapsulation of both hydrophilic and hydrophobic compounds and facilitate an on-demand release [95, 96]. For instance, Wang et al. [96] presented a DNAzyme-driven DNA nanosponge with multivalent aptamers for targeted drug delivery. After being internalized by the target cells, the acidic endolysosomal microenvironment triggered conversions from incorporated ZnO nanoparticles into $Zn^{2+}$ ions, which acted as therapeutic reactive-oxygen-species generators and cofactors for DNAzyme-catalyzed cleavage of DNA scaffolds. DNAzyme-triggered structure disassembly was realized with high efficiency in a moderate concentration of $Zn^{2+}$ ions, suggesting the potential of the nanosponge in practical applications. Likewise, carriers such as aptamer-conjugated DNA self-assemblies can also enable targeted delivery of gene therapies, such as the delivery of siRNA [31, 97], DNAzyme [5], and Cas9/sgRNA (small guide RNA) [98, 99]; in addition, co-deliveries of more than one type of therapeutic agents are also possible [31, 100, 101].

The majority of *in vivo* multivalent aptamer applications are focused on cancer treatment. Over the past decades, many aptamers that specifically target cancer cells have been successfully selected, including AS1411 (nucleolin-targeted) [100, 102], MUC1 (MUC1-targeted) [103], and Sgc8 (protein tyrosine kinase-7-targeted) [15], among others [16, 50]. However, aptamers have not been widely used in *in vivo* cancer treatments. This is likely due to their poor performances under physiological conditions. For example, aptamers are vulnerable to nuclease degradations [104]; in addition, conditions such as temperature [1, 105], pH [106], and shear stress [88, 107] have also been shown to affect the abilities of some aptamers to bind to their targets. As a promising solution to these challenges, multimerizing aptamers can mitigate aptamer instability *in vivo* [108]. For example, Li et al. [39] prepared a self-assembled DNA nanocentipede as a multivalent drug carrier by hybridization chain reaction (HCR). This drug carrier remained intact after treatment with Exonuclease III for 2 hours, thus showing

significantly increased resistance to degradation. Using aptamers in multivalent forms can also maintain or enhance the performance of the aptamer device under physiological temperatures. For example, Mallikaratchy et al. [1] studied the linear molecular assembly of the TD05.1 aptamer, an aptamer specifically targeting B-cell receptors. This group aimed to develop a multimer suitable for *in vivo* applications using as PEG intra-molecular spacers with different lengths. Their findings indicate that the binding ability of TD05.1 monomers were impaired at physiological temperatures, but when connected by PEG with an optimized spacer length, TD05.1 multimers were able to restore some degree of increased avidity.

Another advantage of using multivalent aptamers for *in vivo* applications is their ability to enhance endocytosis. Endocytosis is of interest in understanding the mechanisms that guide the entry of nanomaterials into target cells, which is particularly meaningful for *in vivo* applications [109]. The multivalent effect has been shown to enhance cellular uptake via receptor-mediated endocytosis by improving the local concentration of aptamers [110]. Demonstrating this concept, Kang et al. [111] immobilized multivalent aptamers onto a DNA or a DNA/RNA hybrid structure to build a targeted drug delivery system. For comparison, they separately conjugated dual-type aptamers (AS1411 and MUC-1) and single-type aptamers onto multiple scaffolds of different valency (i.e., monomers, pentamers, nonamers, or RCA generated multivalent scaffolds). The RCA-generated multivalent dual-type aptamer system outperformed monomer aptamer systems with a 2.9-fold higher intracellular uptake in serum-free media.

### 2.3.3. Summary of the recent research

Table 1 summarizes the work on multivalent aptamers in recent years. The table content describes aptamer ingredients, applications, targets, conjugated materials, structures, and advantages of multivalency.

1 **Table 1. A summary of recent published multivalent aptamers related papers**

| Application | Aptamer | Conjugated material | Target | Functional component | Linker/ spacer | Advantages of multivalency | Ref |
|---|---|---|---|---|---|---|---|
| **Spherical multivalent aptamers** | | | | | | | |
| Drug delivery | $SZTI_{01}$ (DNA) | RCA generated spherical DNA self-assembly | Prostate cancer membrane antigen (PCMA)-positive C4-2 cells (PCMA) | Drug loading sites | pH-sensitive oligo-T spacer | Very stable in physiological environment; high specificity | [50] |
| Drug delivery | 5TR1 (DNA) | Poly (lactic-co-glycolic acid) (PGLA) dendrimer; chitosan | MCF7 cancer cells (MUC1 receptor) | Drug loading sites | N/A | High affinity and specificity; good internalization | [16] |

| | | | | | | | |
|---|---|---|---|---|---|---|---|
| Drug delivery | S2.2 (DNA) | Lipid-capped polymer nanoparticle | Cancer cell | Drug loading sites | $PEG_{2000}$ Linker | Significantly higher uptake efficacy; enhanced cell targeting efficiency with increased density of the S2.2 aptamer | [112] |
| Drug delivery | AS1411 (DNA) | Chitosan-silica nanoparticle | SKOV-3 ovarian cancer cell | Drug loading sites | N/A | Higher internalization efficacy | [113] |
| Detection/ Therapeutic | AS1411 (DNA) | AuNPs; Silver nanoclusters (AgNCs) | Cancer cell | Drug loading sites; signaling sequence | Adenine-rich linker sequence | Increased the stability of DNA probe; better internalization | [102] |

| | | | | | | | |
|---|---|---|---|---|---|---|---|
| Detection and isolation | MUC1 (DNA) | Hybrid membrane; $Fe_3O_4$@$SiO_2$ magnetic nanoparticle; $Ag_2S$ | CTC | Signaling component | N/A | Greatly enhanced the anti-interference from background; improve binding ability; good specificity | [81] |
| **Single-layer multivalent aptamers** | | | | | | | |
| Imaging | Sgc8 (DNA) | Manganese dioxide nanosheet | CCRF-CEM cells | N/A | N/A | Target-specific binding and internalization; low background signal; high sensitivity | [114] |

| | | | | | | | |
|---|---|---|---|---|---|---|---|
| Chemo-photothermal therapy | AS1411 (DNA) | Black phosphorus nanosheet | PC3 cells | N/A | N/A | Specific and high photothermal cytotoxicity for target cells | [115] |
| Drug delivery system | C2NP (DNA) | DNA origami | K299 cells (CD30 receptors) | N/A | N/A | Increased internalization; significantly increased aptamer bioactivity | [24] |
| **Linear multivalent aptamers** | | | | | | | |
| Detection | AS1411 (DNA) | RCA generated multivalent chain | B16 cells | Signaling molecular beacon | 18-bp dsDNA intra-molecular spacer | Enhanced sensitivity; enhanced selectivity | [116] |
| Therapeutic | LS Aptamer (DNA) | RCA generated multivalent chain | Jurkat cells (L-selectin) | N/A | 20 oligo-T intra-molecular spacer | High avidity (103-fold higher | [36] |

| | | | | | | | |
|---|---|---|---|---|---|---|---|
| | | | | | | affinity than L-selectin aptamer monomers); high specificity | |
| Detection/cell manipulation | Split ZY11 (DNA) | RCA generated DNA chain | Human liver cancer SMMC-7721 cells | N/A | 41 oligo-T intra-molecular spacer; also served as signaling compartment by hybridization with signaling probe | Improved performance in avidity (a ~2.8-fold increase in signal-to-background-ratio); increased recognition; extended the tolerance range of temperature for target binding | [117] |

| | | | | | | | |
|---|---|---|---|---|---|---|---|
| Detection | CD63 aptamer (DNA) | RCA generated multivalent network | Exosome (surface protein) | Signaling enabled hairpin structure (binding to sequences on the AuNP surface after structural change) | 20 oligo-T intra-molecular spacer | Quantitatively analyses exosomes in the range of $10^5$ to $10^7$ particles per μL | [30] |
| Detection | SYL3C (DNA) | RCA generated multivalent aptamer network electrode interface | CTC (EpCAMs) | N/A | 20 oligo-T intra-molecular spacer | Greatly increased current response; reduced detection time | [7] |

| | | | | | | | |
|---|---|---|---|---|---|---|---|
| Drug delivery | AS1411 and MUC-1 (DNA) | DNA and DNA-RNA hybrid structures | MCF-7 cells | Drug loading site | dsDNA or siRNA duplex as intra-molecular spacer | Increased intracellular uptake of dual aptamer systems (increase in aptamer valency led to higher intracellular uptake) | [111] |
| Detection | Zy1 (DNA) | HCR generated DNA self-assembly | Human liver cancer SMMC-7721 cells | Signaling branch | 10 oligo-T biotin linker; HCR generated backbone spacer | High stability in the presence of nuclease or in human serum; higher signal-to-background | [118] |

| | | | | | | | |
|---|---|---|---|---|---|---|---|
| | | | | | | ratio compared with aptamer monomers; reduced dissociation constant (1/10) compared with Zy1 monomers | |
| Drug/siRNA delivery | Mucin-1 (DNA) | BLC2-specific siRNA | MCF-7 breast cancer cells | BCL2 siRNA; drug loading site. | siRNA duplex intra-molecular spacer | High intracellular uptake efficiency; high specificity | [31] |
| **Others** | | | | | | | |
| Drug delivery | Sgc8 (DNA) | DNA origami generated self-assembly (triangular) | Cancer cell/HeLa cell | Drug loading sites | N/A | Enhanced drug delivery efficiency and therapeutic | [49] |

| | | | | | | | |
|---|---|---|---|---|---|---|---|
| | | | | | | efficacy; decrease systemic toxicity; high stability in cell culture medium for 24 h | |
| Targeted gene therapy | Sgc8 (DNA) | AAV2 vectors | CCRF-CEM cells (PTK7) | AAV2-Based Vectors | DNA dendrimer linker | 21-fold enhanced binding affinity and enhanced resistance against nuclease degradation | [4] |
| Immunotherapy | KK1B10 (DNA) | HCR generated DNA self-assembly-functionalized | K562 cells | N/A | HCR generated backbone spacer | Greatly increased binding avidity than the | [107] |

| | | | | | | | |
|---|---|---|---|---|---|---|---|
| | | natural killer cells | | | | aptamer monomers; good stability under physiological shear stress | |
| Detection and capture | ZY-sls (DNA) | Cell imprinted hydrogel | SMC-7721 cells | N/A | Trifunctional cleavable cross-linker | Enhanced interaction between enhanced sites and target cells; high capture efficiency and selectivity; 92% of the captured cells could be released | [43] |

2

## 2.4. Rolling circle amplification: strategies of design and optimization

In general, three steps are involved in an RCA reaction: synthesis of circular probe template; hybridization of a primer to the circular probe template; and primer-initiated ssDNA elongation, as shown in Figure 7. The design of the two nucleotide sequences, namely a linear single-stranded padlock probe and a primer, are of importance for an efficient RCA reaction.

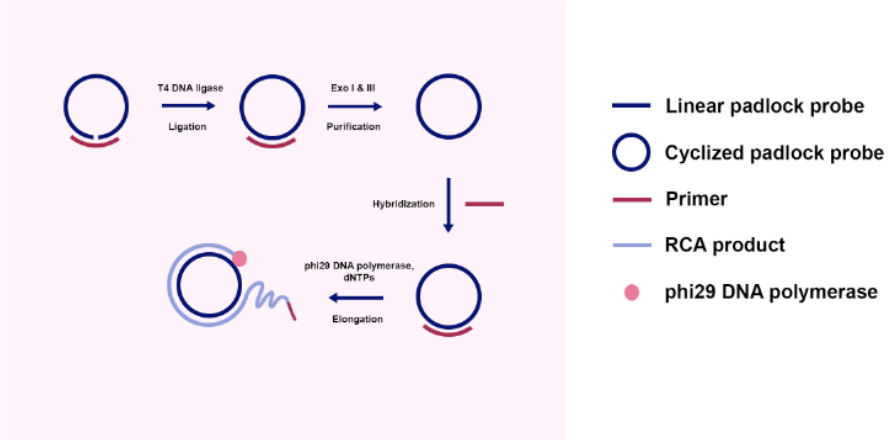


Figure 7. The progress of an RCA reaction.

### 2.4.1. Strategies to enhance the yield of RCA product

*2.4.1.1. Factors improving cyclization efficiency*

Cyclization yield refers to the production of circular probe template from the initial substrates. High cyclization yield is ideal for enhancing the yield of RCA products. The most widely applied enzymatic synthesis of cyclized probes faces issues such as high cost and difficulty of scaling up. Length of the linear probe is tightly related to the cyclization efficiency. An et al. [119] suggested in their work that a linear probe of 30 to 45 nt can lead to poor cyclization yield due to structural constrain resulting from the short length of the probe, while a probe of excessive length (*i.e.*, more than 72 nt) can result in by-product formation [120]. When the length of a linear probe exceeds 100 nt, the possible preparation methods are limited, mainly due to the

difficulties of long linear probe synthesis and the significant formation of by-products due to inter-molecular hybridization of multiple linear probes and primers [121]. An alternative method is to join multiple linear probe segments progressively. In this case, relatively large size circular probe templates can be synthesized from two precursor segments since preparative yields for dimeric synthesis is greater than those from single precursors [122].

Single-stranded DNA has been reported to form secondary and tertiary structures through base-pairing or stacking interaction, which can influence the cyclization efficiency either negatively or positively. For instance, Cui et al. [123] found that cyclization efficiency is poor when the linear probe has a complicated secondary structure. They solved this problem using Taq DNA ligase at 65-70 °C, which destabilizes secondary structures. In addition, the same group also demonstrated the relationship between cyclization efficiency and the presence of hairpin structures at the terminal of the linear probe when treated with T4 DNA ligase [120]. Oligonucleotide terminal hairpins prefer to cyclize intramolecularly rather than polymerize intermolecularly. The cyclization of oligonucleotides with a hairpin near either of its 3’ or 5’ ends proceeded predominantly through intramolecular cyclization with high selectivity. The terminal hairpin strategy also applies to CircLigase.

Other strategies for enhancing cyclization efficiency include adding external components into the ligation solution. For example, poly(ethylene glycol) (PEG) macromolecules can facilitate DNA-protein interaction by providing a molecule-crowded environment, thereby improving T4 DNA ligase/polymerase, T7 polymerase, and Taq polymerase activities [124, 125]. The mechanism of such an improvement is believed to be due to the enhancement of the cyclization of probes rather than facilitation of the progression abilities of DNA polymerase [125]. RCA products were

reduced when PEG was used in RCA product elongation due to the fact that crowding facilitates hybridization, which suppresses de-hybridization and thus primer extension.

*2.4.1.2. Factors effecting amplification efficiency*

For RCA-based applications, a constant amplification efficiency without significant bias under various conditions is important. Joffroy and coworkers [10] found a template length-dependent amplification efficiency bias of RCA with the same periodicity using two types of DNA polymerases: phi29 and Bst 2.0. Their results showed that when designing a probe, one should ensure that the length of the probe should be chosen within the size range of the periodic maxima, and shorter probes performed better than longer ones in general. The results also concluded that changing the template size of the linear probe, even by as little as 5 nt can significantly influence the obtained results. The researchers concluded that the potential molecular mechanism behind this bias is a changing fraying probability dependent on the conformation of the DNA-polymerase complex.

*2.4.1.3. Exponential RCA*

Exponential RCA (E-RCA), in contrast to linear RCA, is exponential amplification initiated by a single binding event between a primer and a cyclized probe. This is achieved by the introduction of extra primers and/or nicking enzymes into the RCA system. Incorporation of exponential components significantly enhances the efficacy of RCA reactions. Various types of exponential RCA include multi-primed [126], multi-branched (mbRCA) [127], hyper-branched (HRCA) [128], circle-to-circle (C2C RCA) [129], and primer-generated (PG-RCA) RCA [130], as summarized in Figure 8. For instance, the amplification can be enhanced a million-fold using HRCA by incorporating a second reverse primer [131]. Due to its intrinsic rapid nature, exponential RCA is widely applied as a signal amplification technique for detecting microRNA

[132], single nucleotide polymorphisms (SNP) [131], and DNA [133]. The detection sensitivity of E-RCA has been demonstrated to be 100-fold higher than that of PCR [134].

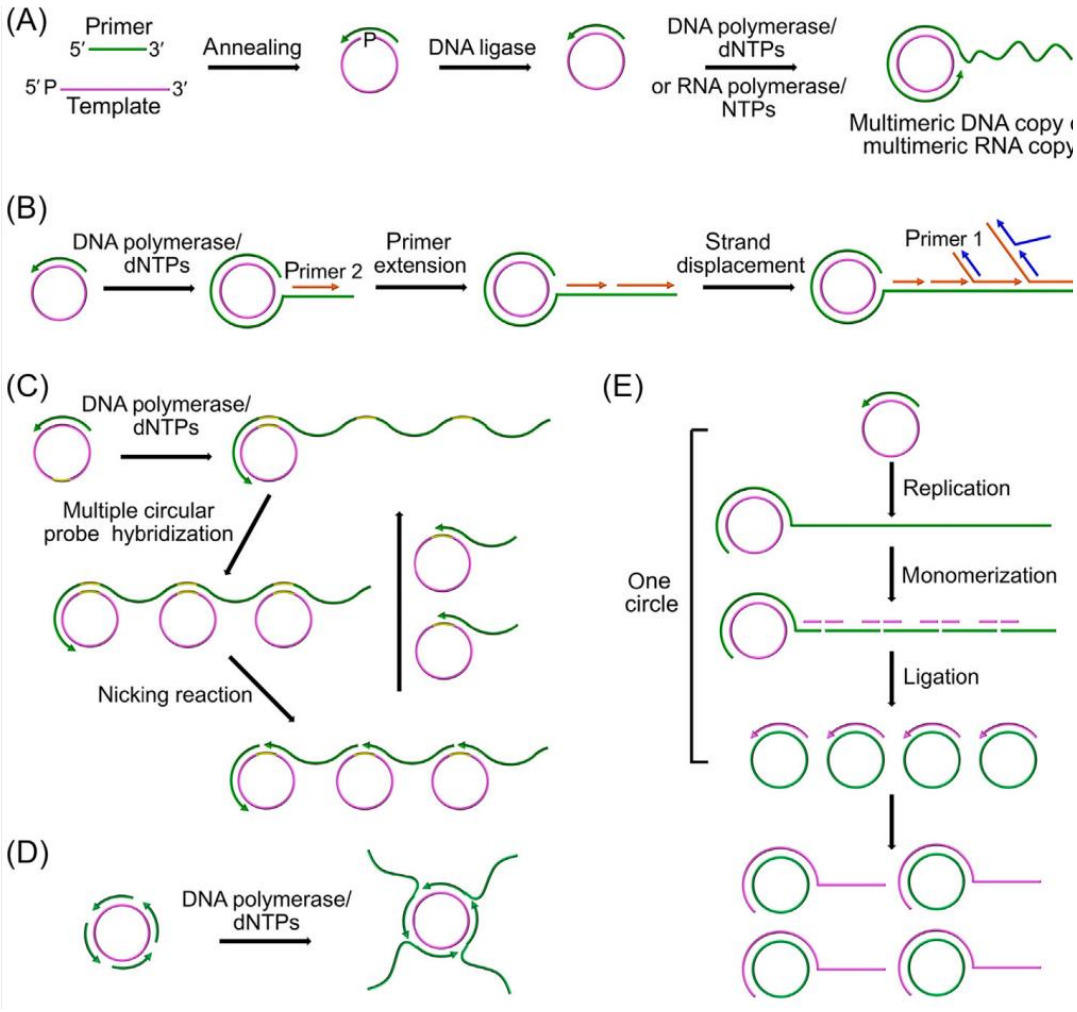


Figure 8. Principles of linear and exponential RCA. Schematic diagram of (A) Linear RCA. (B) HRCA. (C) PG-RCA. (D) multiply-primed RCA. (E) C2C RCA. (ref. **[135]**)

Recent studies have combined two types of E-RCA to achieve even greater amplification. For instance, Zhu et al. [131] developed a netlike RCA by introducing a nicking enzyme into the hyperbranched RCA system for detecting single nucleotide polymorphism (SNP). This quadratic amplification technique has much higher efficacy than HRCA, reaching a detection limit of 5.4

aM of the target molecule. Moreover, DNAzyme feedback amplification mechanisms (DFA) can also be coupled with RCA to achieve an exponentially enhanced efficacy [136, 137]. In brief, the presence of the target triggers an RCA reaction, which produces repeated copies of DNAzyme. These DNAzymes cleave specific sites of an RNA-containing portion of RCA product, producing additional primers that hybridize with the cyclized probe as new inputs for RCA.

### 2.4.2. Structure of the RCA product

The morphology of the RCA product can influence the performance of RCA-based applications. The morphology of RCA products can be tuned by applying various designs and strategies. Recent works in nanomaterials take advantage of the rapid nature of RCA to produce long ssDNA chains containing hundreds or thousands of aptamer repeats (multivalent aptamers) to achieve higher binding avidity. These applications rely on the RCA product being single-stranded, with their performance being dependent on RCA product conformation. It is important to note that multivalent aptamer chains showed decreasing trends in capturing ability when the RCA reaction time exceeded a certain limit (i.e., 60 min [6]). This observation is suggested to be caused by the higher inter- and intra-molecular interactions that occur when RCA products of excessive length or density were produced. As demonstrated by Li et al., with longer RCA reaction time, tangled morphologies in RCA products could inhibit product-target binding due to unwanted structures [138]. Xie et al. [139] also showed that RCA products tend to intertwine into micro-scale coils, decreasing the number of effective binding sites and lowering capture efficiency. Heat-activation can be used as a solution: using this strategy, multivalent aptamer chains were stretched into nano-strands, leading to significantly enhanced efficiency (from 5.29% to 86%) [139].

With respect to template design, incorporating a complementary sequence of homo-oligonucleotides such as polyT can also be an alternative solution to solve inter- and intra-molecular structure tangling in RCA products [6]. Resultant RCA products would carry a long polyT motif disfavoured in DNA hybridization, thereby avoiding the misfolding of adjacent aptamers and improving the accessibility and probability of association of the aptamer binding motif to the target [140]. In addition, adding short DNA probes complementary to specific repeated motifs can stretch the RCA-generated nanochain [141]. Hybridization of the spacer domain with its complementary oligonucleotide between aptamer domains enables the function of aptamer-decorated DNA strands, likely by extending the RCA products, thereby minimizing nonspecific base-pairing with the aptamer domains [6].

In comparison, RCA-based nanomaterials such as DNA nanoflowers require the RCA products to have condensed morphologies and smaller size for more efficient cellular uptake. Studies investigating the conformation of RCA-generated nanoflowers using different template probe sequences also confirmed the previously mentioned principle about polyTs containing products—compared with polyT containing products, the size of the resultant nanoflower without polyT showed a significantly smaller hydrodynamic size. This was suggested to be caused by the secondary structure-forming sequences, which allow long DNA chains to be folded into a smaller space [142, 143]. More complex structures such as tertiary G-tetrads can provide additional packing levels for nanoflowers [143]. These researchers also demonstrated that RCA-generated nanoflower sizes can be tuned by adjusting template sequences as well as by adding modified nucleotides [143, 144].

# Chapter 3. Experimental

## 3.1. Materials

Polydimethylsiloxane (PDMS) Sylgard 184 kit was purchased from Dow Corning (Midland, Michigan). Poly(amidoamine) dendrimer (generation 6.5, PAMAM-COOH) was purchased from Dendritech (Midland, MI). N-Hydroxysuccinimide (NHS), (3-Aminopropyl) triethoxysilane (APTES), nuclease-free water, and N,N,N',N'-Tetramethylethylenediamine (TEMED) were purchased from Sigma-Aldrich (Oakville, ON). 1-(3-dimethylaminopropyl)-3-ethylcarbodiimide (EDC) and 2-(N-morpholino) ethanesulfonic acid (MES) were purchased from Alfa Aesar (Ward Hill, MA). DNA oligonucleotides (sequences shown below) and IDTE (1× TE) buffer were purchased from Integrated DNA Technologies (Coralville, IA). phi29 DNA polymerase, 10× reaction buffer for phi29 polymerase, T4 DNA ligase, 10× T4 ligation buffer, deoxynucleotide triphosphate (dNTP) solution mix, ammonium persulfate (APS), 10×TBE (Tris/Borate/EDTA) electrophoresis buffer, acrylamide solution (containing 40% (w/v) of acrylamide (38%) and bis-acrylamide (2%)), nucleic acid loading buffer (Cat #: LC6678; SM0242), DNA ladders (Cat #: 10597012), SYBR Gold nucleic acid gel stain, Exonuclease I and III (Exo I and III), and 10× exonuclease buffers were purchased from Thermo Fisher Scientific (Burlington, ON). Heat-killed fluorescein isothiocyanate (FITC) labeled target *E. coli* O157:H7 cells and nontarget *E. coli ATCC25922* were generous gifts from Canada Food Inspection Agency (Ottawa, ON). All other chemicals were obtained from VWR International, LLC Canada unless indicated otherwise. DNA sequences are listed below:

Table 2. The sequence of DNA oligos that was used in this study

| **Name** | **Sequence (5'—>3')** | **Ref.** |
|---|---|---|
| E17F-72 aptamer | ATCCG TCACA CCTGC TCTAT CAAAT GTGCA GATAT CA**AGA CGATT TGTAC AAG**AT GGTGT TGGCT CCCGT AT | [145] |
| NT-primer | $NH_2$-TTTTT TTTTT TTGGC TCCCG TATAT CCGTC ACACC T | This work |
| 5T-primer | $NH_2$-TTTTT TTTTT TGTTG GCTCC CGTAT TTTTT ATCCG T | This work |
| 10T-primer | $NH_2$-TTTTT TTTTT TGTTG GCTCC CGTAT TTTTT TTTTT A | This work |
| 15T-primer | $NH_2$-TTTTT TTTTT TGTTG GCTCC CGTAT TTTTT TTTTT T | This work |
| NT-linear probe | Phos-*ATACG GGAGC CAACA CCATC TTGTA CAAAT CGTCT TGATA TCTGC ACATT TGATA GAGCA GGTGT GACGG AT* | This work |

| | | |
|---|---|---|
| 5T-linear probe | Phos-*ACGGG AGCCA ACACC ATCTT GTACA AATCG TCTTG ATATC TGCAC ATTTG ATAGA GCAGG TGTGA CGGAT* AAAAA *AT* | This work |
| 10T-linear probe | Phos-*ACGGG AGCCA ACACC ATCTT GTACA AATCG TCTTG ATATC TGCAC ATTTG ATAGA GCAGG TGTGA CGGAT* AAAAA AAAAA *AT* | This work |
| 15T-linear probe | Phos-*ACGGG AGCCA ACACC ATCTT GTACA AATCG TCTTG ATATC TGCAC ATTTG ATAGA GCAGG TGTGA CGGAT* AAAAA AAAAA AAAAA *AT* | This work |
| Cy3-fluoresence probe | Cy3-TTTT**C TTGTA CAAAT CGTCT** | [138] |

Note: The italic portion in the linear probe is complementary to the sequence of aptamer that binds to the polysaccharide residues on *E.Coli* O157:H7 surface; the underlined portions in primer and linear probe are used for probe-primer hybridization. The **bold** portion in Cy3-fluoresence probe is partially complementary to the RCAP.

## 3.2. Methods

### 3.2.1. General approach

This study investigates the effect of polyT spacer length on the capturing performance and morphology of resultant RCAP. As shown in Figure 9, the inner surface of a PDMS microchannel is first engrafted with generation 6.5 (G6.5) PAMAM dendrimer using our previously developed NHS/EDC coupling method [93]. Subsequently, the carboxyl functional groups of PAMAM dendrimer are activated, followed by the conjugation of 5' amine-modified primer. After incubating with the pre-synthesized circular probe template, *in situ* RCA [138, 146] is performed by injecting the RCA mixture containing phi29 polymerase, phi29 buffer, and dNTP. The RCA reactions are performed for a pre-determined period to produce a fixed number of aptamers on the amplified DNA chains (*i.e.,* RCAPs), that are complementary to the circular probe template in a head-to-tail manner. The capturing performances of the resultant microchannels are then tested.

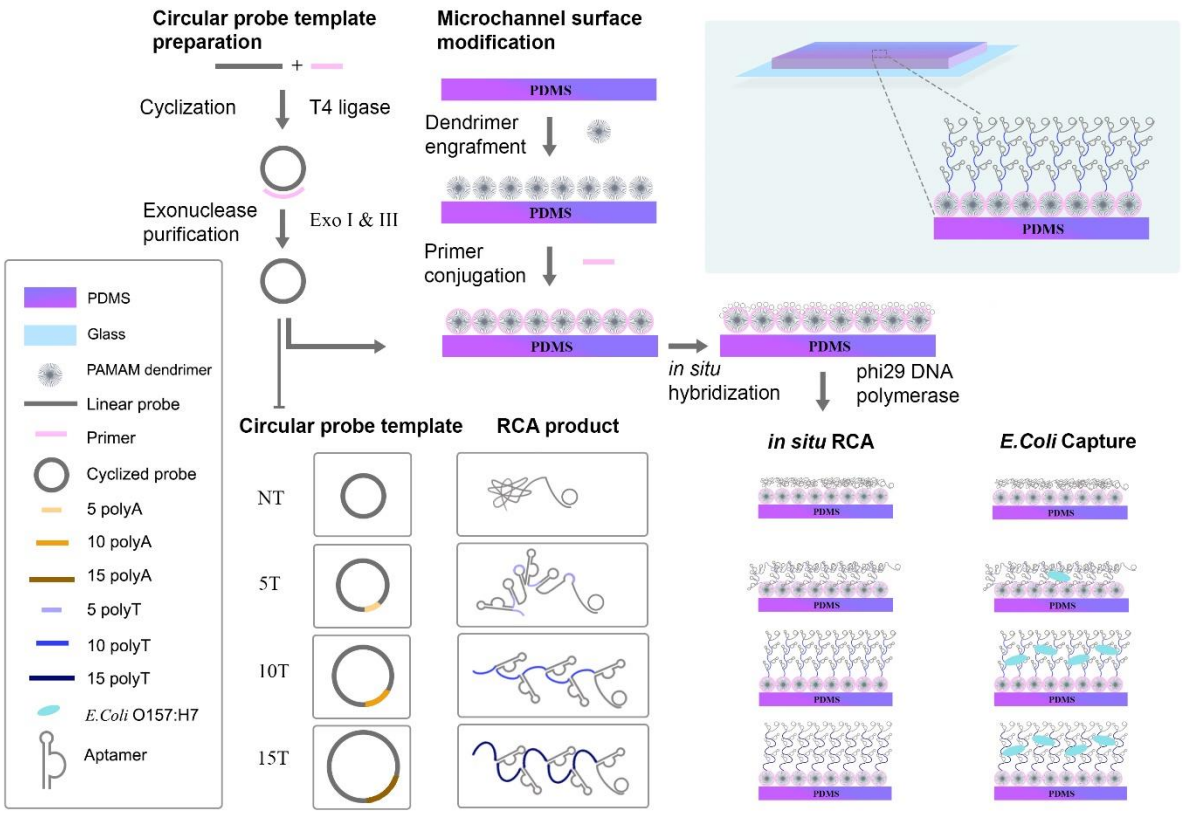


Figure 9. A schematic diagram for overall experimental procedure for fabricating RCAP-PAMAM dendrimer-modified PDMS microfluidic device, RCAP morphology, and target cell *E.Coli* O157:H7 capture.

### 3.2.2. Circular probe template preparation, characterization of reaction products and cyclization efficiency

To prepare and purify the circular probe template, different pairs (i.e., NT, 5T, 10T, and 15T) of linear probe and primers (100 µM, 1.5 µL each) was mixed in 23.4 µL nuclease-free water. The mixture was first heated to 95°C for 10 min to completely eliminate the intrinsic secondary structures of the linear probes, quickly ice-cooled for 1 min, and hybridized at 37°C for 30 min (heat treatment). Subsequently, T4 ligase (10U) and 3 µL ligation buffer were added to the reaction mixture, and the ligation reaction was carried out for 1 hour before it was deactivated at 65°C for 10 min. To purify the resulting circular probe templates, Exo I (1U/µL) and III (1U/µL)

in 3 µL Exo buffer were added to the cyclized products at 37°C for 2 h in order to remove any remaining free primers, uncyclized probes, and undesirable linear by-products, after which the exonucleases activities were deactivated at 85°C for 15 min. Finally, the circular probe templates were purified by ethanol precipitation [143] and stored in nuclease-free water for future use. To characterise the cyclization yield, the circular probe templates (i.e., NT, 5T, 10T, and 15T) were prepared as described above. The amount of each of the resulting circular probe templates were characterized using 8% poly(acrylamide) gel electrophoresis (PAGE) by a Min-PROTEAN Tetra System (Bio-Rad Laboratories, Hercules, CA). Subsequently, the gel was stained in 1× TBE buffer with 1× SYBR Gold nucleic acid dye. The gel images were acquired using ChemiDoc XRS+ system (Bio-Rad Laboratories, Hercules, CA) and analyzed by ImageLab V6.0.1 (Bio-Rad Laboratories, Hercules, CA).

### 3.2.3. Characterization of amplification rate using gel shift assay

To investigate the amplification rate of RCA reactions, a PAGE gel shift assay (i.e., probe hybridization assay) was used to estimate the rate of amplification (i.e., the number of tandem aptamers produced) in an RCAP multivalent aptamer chain [147]. Briefly, an RCA mixture containing 0.01 µM circular probe template, 1× phi29 reaction buffer, 0.1 U/µL of phi29 DNA polymerase, and 400 µM of dNTPs was carried out at 37°C. At pre-determined RCA reaction time points (i.e., 10 min, 20 min, 30 min, 40 min, 50 min, and 60 min), single-stranded Cy3-labeled fluorescent probes with complementary sequence (see Table 2, 5 µM) were added into the RCAP. The resultant mixture was heated to 95°C and was then incubated at 37°C for 1 h to maximize probe-RCAP hybridization prior to PAGE analysis; subsequently the fluorescence intensities of the PAGE bands were measured by ImageLab V6.0.1.

### 3.2.4. Microchannel fabrication and PAMAM dendrimer engraftment

To fabricate the PDMS microchannel, Sylgard 184 elastomer and curing agent were mixed thoroughly at a 10: 1 ratio (w/w). The mixture was quickly placed on a SU-8 master, degassed for 1 hour, cured at 85°C for 2 hours, and cooled down to room temperature. Subsequently, the cured PDMS layer was gently peeled off from the master, punctured with two holes at either side of the microchannel as the inlet and the outlet, rinsed with 99% ethanol and double-distilled water ($ddH_2O$), and finally air-dried. The cleaned PDMS surface was treated with oxygen plasma using a plasma etcher (SP100, Anatech Ltd, Battle Creek, MI) at 100 m Torr, 118 W for 10 s, and the resultant surface was immediately sealed with a glass slide by applying constant pressure and temperature (95°C for 5 min) [93]. To conjugate PAMAM dendrimer onto the inner surface of the microchannel, a previously established silane coupling method was used with minor modifications [84, 146]. Briefly, 5 wt.% APTES in anhydrous ethanol was used to treat the microchannel for 20 s in order to animate the inner surface by silanol condensation. This step was followed by a gradient wash with absolute ethanol, 95% ethanol, 70% ethanol, and $ddH_2O$. Finally, 5 µM PAMAM dendrimer was pre-activated by 0.1 M NHS and 0.1 M EDC in 0.1 M MES solution (pH 6.0) for 15 min, and the resultant solution was injected into the aminated microchannel at room temperature for 1 h to achieve dendrimer engraftment on the inner surface of the PDMS microchannel.

### 3.2.5. *In situ* RCA on microchannel inner surface

The RCA reaction comprises three steps: preparation and purification of circular probe template, conjugation of primer and circular probe template onto the microchannel surface, and initiation of *in situ* RCA reaction inside the microchannel. To conjugate the purified circular probe

template, the dendrimer-engrafted microchannel was first treated with 0.1 M NHS and 0.1 M EDC in 0.1 M MES solution (pH 6.0, salt-free) for 30 min to activate the surface carboxyl groups. Subsequently, 1 μM 5' $NH_2$-capped primer was injected into the channel and allowed to react for 1 h. Then the purified circular probe template was injected into the microchannel at 37°C and incubated for 1 h. For *in situ* RCA reaction, the RCA reaction mixture containing 1× phi29 buffer, 0.4 mM dNTPs, and 10U phi29 polymerase was injected into the microchannel at a flow rate of 0.05 mL/h. The reaction was allowed to be carried out at 37 °C for a pre-determined period of time, after which the microchannel was heated to 65 °C for 5 min to deactivate phi29 polymerase, and the microchannel was carefully rinsed with PBS (pH 7.4).

### 3.2.6. Water contact angle measurement

To confirm layer-by-layer surface modifications, water contact angles of surfaces of interest (i.e., PDMS surface, APTES modified surface, PAMAM-immobilized surface, NT, 5T, 10T, and 15T RCAP-modified surfaces) were measured using a goniometer (AST Products Inc., Billerica, MA). Three random measurements were taken on each sample surface, on a total of three sample surfaces, and the average values were reported.

### 3.2.7. Microchannel capturing performance for target *E.Coli* O157:H7 cells

To evaluate the capturing performance of RCAP modified microchannels for *E. coli* O157:H7, FITC-labeled target cells ($1 \times 10^5$ cells/mL) were introduced into the capturing microfluidic channels at a flow rate of 0.05 mL/h, after which the channels were carefully rinsed with PBS (pH 7.4) at a flow rate of 0.1 mL/h. The captured cells were documented using an Olympus fluorescence microscope (IX81, Richmond Hill, ON). For each microchannel, sixty continuous

fluorescent images were collected and the number of captured cells was analyzed by NIH ImageJ software (NIH, Bethesda, MD).

### 3.2.8. Fluorescence intensity measurement of RCAP-conjugated surface

To demonstrate the success of the RCA reactions on the PDMS surfaces, *in situ* RCA reactions were carried out as outline in Section 3.2.5. The resulted microchannel surfaces were incubated with 2 μM of Cy3-labeled fluorescent probes that are partially complementary to the aptamer sequences of the RCAPs. The fluorescence intensity was documented using a high-resolution camera (QImaging, Surrey, BC) and analyzed using NIH ImageJ. On each sample surface, five spots were randomly selected, and the fluorescence intensities were measured. The average fluorescence intensity value from each sample surface was calculated and reported.

### 3.2.9. Characterization of dendrimer conjugated RCAP by dynamic light scattering

In order to investigate the morphological characteristics of the RCAPs as a result of different circular probe template designs, different designs of circular probe templates were used to initiate RCA reactions on the surfaces of free PAMAM dendrimers – as opposed to PAMAM dendrimers immobilized to PDMS surfaces – to allow characterization by dynamic light scattering (DLS). For each of the circular probe template, RCA reaction times were controlled so that the resulting RCAPs would have same number of repeating aptamer units (i.e., same number of amplifications). In preparing the samples for the DLS characterizations, 60 μL of PAMAM-conjugated RCAPs were diluted in 600 μL of 1×TE buffer. The DLS measurements were performed using a Zetasizer Nano ZS (Malvern Panalytical, Malvern, UK), and the acquired data were processed using Zetasizer Software V7.12 (Malvern Panalytical, Malvern, UK).

### 3.2.10. Fluorescence intensity measurement of RCAP

To test the fluorescence intensity of RCAP, 10 µL of 0.5 µM RCAP was diluted in 40 µL of nuclease-free water. Afterward, ethidium bromide (EtBr, final concentration 0.5 µg/mL) was added to the sample and mixed thoroughly. The fluorescence intensities of the resultant samples were measured in 96-well plates using Synergy H1 microplate reader (BioTek Winooski, Vermont) with the following parameters: excitation, 285 nm; emission, 605 nm, as suggested elsewhere [17]. The acquired data were processed by Gen5 Software V3.09.07 (BioTek, Winooski, Vermont).

### 3.2.11. Statistical analysis

To determine whether there are significant differences between the four test groups (NT, 5T, 10T, and 15T), the results in cyclization yield, water contact angle, capturing performance, surface fluorescence intensity, hydrodynamic size, and RCAP fluorescence intensity of no spacer test group (NT) and three spacer test groups (5T. 10T, and 15T) were firstly analyzed using One-way ANOVA test (Brown-Forsythe and Welch ANOVA, without assuming equal standard deviation). If the result of One-way ANOVA test reveals significant differences, then the above-mentioned results of each spacer test group was individually grouped and analysed with no spacer test group (NT) using unpaired t-test with Welch's correction (without assuming equal standard deviation) for testing whether a significant difference exists between no spacer test group (NT) and each of spacer test groups (5T, 10T, and 15T). All data were analyzed using GraphPad Prism 8.4.2 (GraphPad Software, San Diego, CA).

# Chapter 4. Results and Discussion

## 4.1. Characterization of circular probe templates and RCAPs

To demonstrate the progression of RCA reaction, the starting materials and the products from each reaction stage were characterized using 8% PAGE. Figure 10 shows the gel images of the primers (Lane 1), linear probes (Lane 2), cyclized products before (Lane 3) and after (Lane 4) Exo I & III purification, circular probe templates hybridized with primers (Lane 5), and RCAPs based on four different circular probe templates (*i.e.,* NT, 5T, 10T, and 15T) (Lane 6), respectively. Lane 3 in each gel image shows the cyclized products includes the circular probe template and various by-products, and Lane 4 shows pure circular probe templates, which is also confirmed by their resistance to Exo I & III digestion [120, 148]. These circular probe templates are located at lower positions in comparison with their respective linear probes (Lane 2) although they are of identical lengths. This can be explained by their structural (i.e. circular vs. linear) differences [149]. Because of the different length of adenine bases in the designed linear probes (and therefore a difference in probe total lengths), the resultant circular probe templates show an increasing molecular weight, as demonstrated by gradually higher band positions (indicated by white arrows in Land 4s). Lane 5s show that after hybridizing the circular probe templates with the primer, the band shifts up back to the position of the band with highest intensity in Lanes 3s (indicated by purple arrows). Lane 6s show the RCA products after 30 min, suggesting the presence of high molecular weight products that were unable to migrate out of the electrophoresis wells. It should be noted that the DNA ladders used in this experiment are designed for dsDNA, and as a result the molecular weights indicated by the ladders are not the true molecular weights of the ssDNA molecules of interest [146].

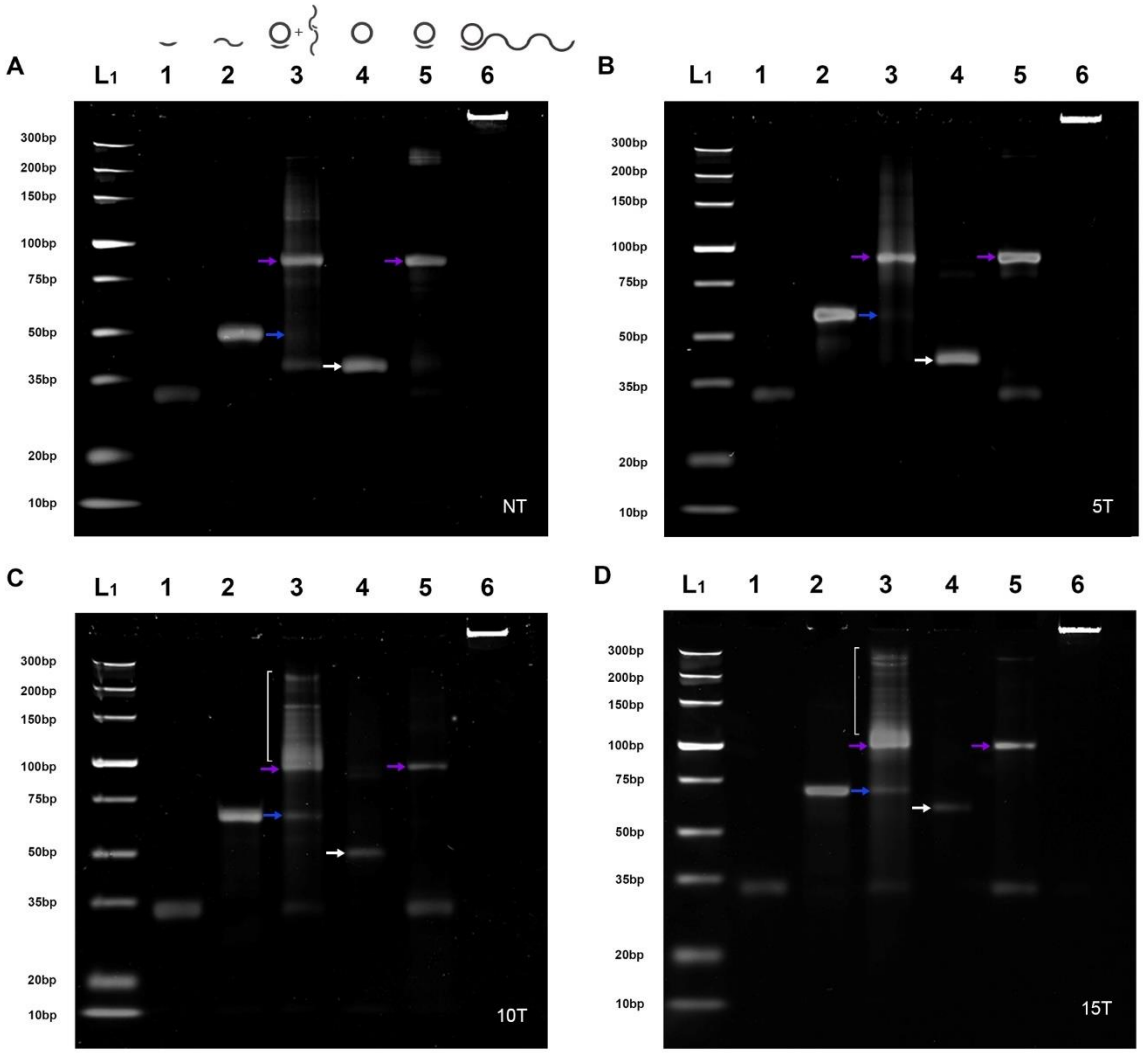


Figure 10. Gel image of primer, linear probe, and resultant products in each step of RCA reaction of NT, 5T, 10T, and 15T template (A to D), respectively. Samples were resolved in an 8% native PAGE gel. Lane L1: DNA ladder; Lane 1: primer; Lane 2: linear probe. Lane 3-5: resultant products of probe cyclization. Lane 3 represents the unpurified cyclization product; Lane 4 shows the circular probe template after exonuclease purification; Lane 5 shows the hybridized product of circular probe and primer. Lane 6 shows the RCAP after 30 min, initial template concentration = 0.1 µM. The white arrows indicate the circular probe template; the blue arrows indicate the presence of uncyclized linear probe in cyclization products; the purple arrows indicate the hybridized primer and circular probe template.

## 4.2. Calculation of cyclization yield

The production of circular probe templates can vary largely due to the design difference of the original linear probes. To estimate the yield of circular probe template generated by four different designs, a DNA hybridization assay was used based on the principle that the circular probe template and primer hybridized in an 1 : 1 ratio. The process of the hybridization assay is shown in Figure 11. As shown in Lane 1, after purification, the circular probe template without primer appears as a single intense band. After hybridizing with primers (Lane 2), this respective band disappeared, suggesting the complete consumption of circular probe template during the hybridization process, while a new single band representing the primer + purified circular probe template complex appeared. This single up-shifted band was expected because we designed our primer and circular probe template in a way that there is only one hybridization region between the two probes. The lower band in Lane 2 represents the residual primer after the hybridization assay. Lane 3 represents the primer before the hybridization assay, which composes a standard curve for calibration together with diluted premiers in Lanes 4-7.

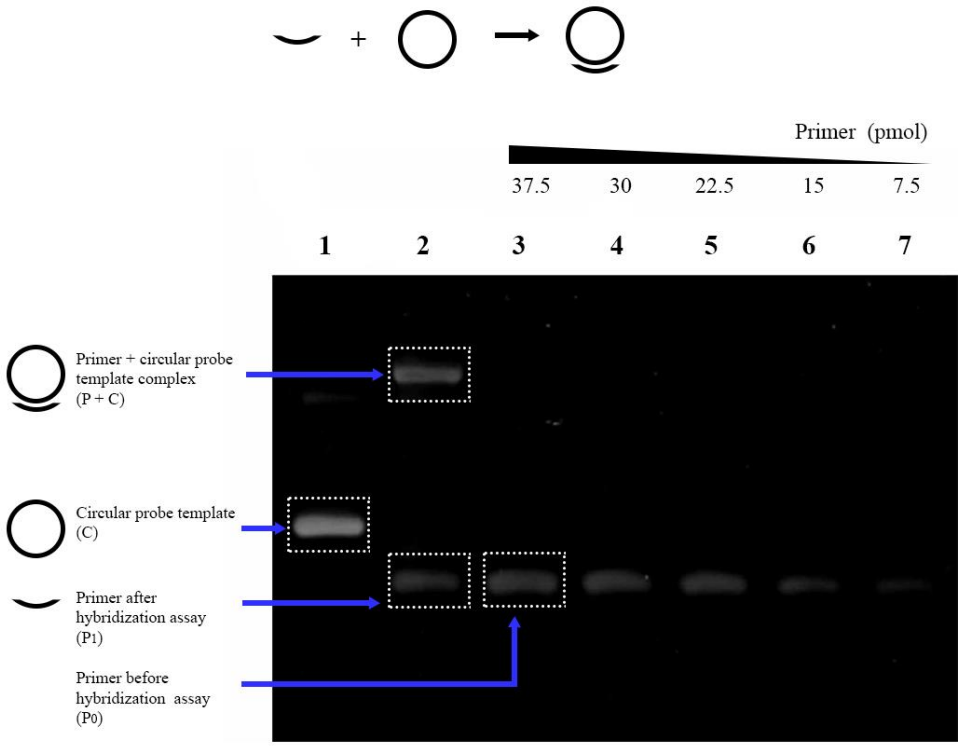


Figure 11. A schematic illustration showing the principle of using DNA hybridization assay on PAGE for cyclization yield calculation.

Due to the 1 : 1 ratio of primer - circular probe template hybridization, the amount of circular probe template was estimated by the difference (i.e., the up-shifted primer) between primer band intensity before and after the hybridization assay using the following equation:

$$C = P = P_0 - P_1,$$

where $C$ refers to the amount of circular probe template, $P$ refers to the amount of up-shifted primer, $P_0$ and $P_1$ represent the amount of primer before and after hybridization, respectively ($P_0$ - $P_1$ equals the difference in band intensities of Lane 3 and Lane 2). As a basis of comparison, the fluorescence intensities of primers of different known amounts (shown in Lane 3 to Lane 7, *e.g.*,

37.5 pmol, 30 pmol, 22.5 pmol, 15 pmol, 7.5 pmol) were analyzed using ImageLab to generate a calibration curve. Afterwards, $P_0$ and $P_1$ were calculated by using the "absolute mode" of quantity tools in ImageLab. After obtaining the amount of circular probe template, the cyclization yield was calculated as:

$$\textit{Cyclization yield (\%)} = C/L \times 100,$$

where $L$ refers to the corresponding initial amount of linear probe.

The One-way ANOVA test reveals that significant differences exist in cyclization yield among NT, 5T, 10T and 15T templates (p-value < 0.0001). By incorporating zero to fifteen polyA bases), a decline in cyclization yield was observed between no spacer test group and each of the spacer test groups. The cyclization yields are 48.12 ± 2.69 %, 31.57 ±2.60 %, 24.73 ± 2.28 %, 14.38 ± 4.18 % for NT, 5T, 10T, and 15T, respectively (Figure 12). Our results coincide with the results obtained by Liang's group [119] that when the length of the linear probe exceeds a certain range (*e.g.,* over 70 nt), longer probe length can impair the production of circular probe templates. This observation can be explained by the preferable formation of by-products. Instead of intra-molecular cyclization, longer linear probes prefer inter-molecular hybridization, which leads to the joining of several linear probes with primers to form larger polymers [119, 120], shown as the multiple bands in Lane 3s in Figure 10, especially C and D (indicated with brackets). In addition, as adding longer polyA into the original linear probe, a visible band with higher intensity was observed (Figure 10 A to D, Lane 3, indicated by blue arrows), revealing the presence of unhybridized linear probe in the cyclization products. This observation indicates that the impairment of cyclization yield can also be caused by the inefficient hybridization of the primer and the linear probe.

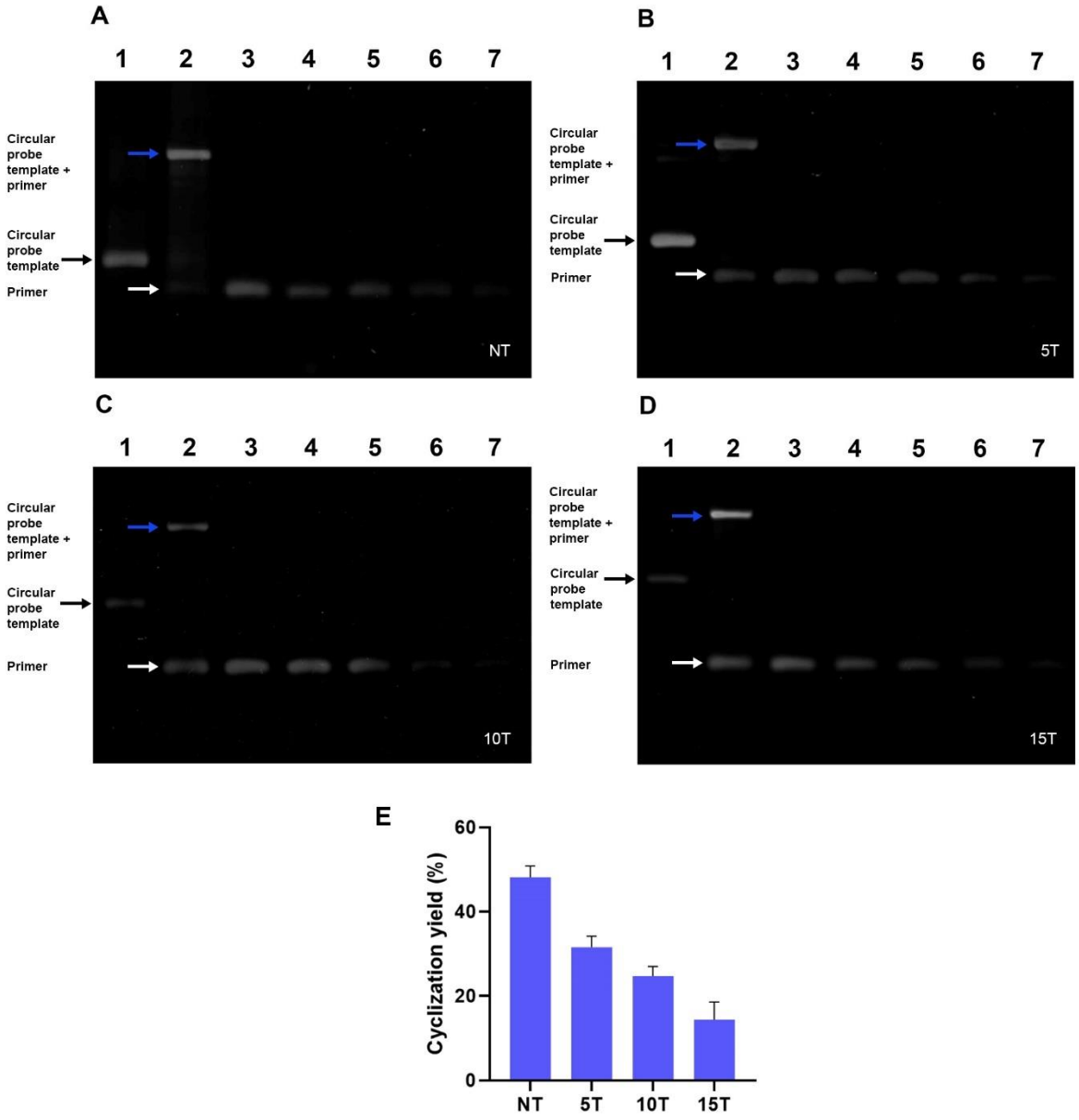


Figure 12. Hybridization assays of DNA for calculating the cyclization rate of (A) NT, (B) 5T, (C) 10T, and (D) 15T. Lane 1: purified circular probe template. Lane 2: circular probe template hybridized with a known amount of primer. Lane 3-7: primers with standard amounts. (E) shows the cyclization yields calculated using the equation in Section 3.2.2. Error bars indicate the standard deviations (n = 3). The white arrows indicate the unhybridized primer; the blue arrows indicate the hybridized primer + circular probe template.

### 4.3. Evaluation of RCA amplification rate

To estimate the quantity of tandem aptamers as the RCA reaction progresses (i.e., the amplification rate), we applied the method from a previously published study [147]. In brief, a gel shift assay was performed by adding a Cy3-labeled fluorescent probe to the RCAP (the existence of RCAP in the samples was proven in Figure S1, a schematic drawing is shown on the left side of Figure 13 A) after terminating the RCA reaction at different time points. The fluorescence intensity of the free Cy3-probe band (indicated by the lower black arrow in Figure 13 A to D) gradually decreased as the reaction proceeded, which is consistent with the increase of upper band intensity caused by the hybridization between upward shifted Cy3-probes and RCAP. The fluorescence intensities of the Cy3-probe were measured and analyzed using the "relative mode" of quantity tools of ImageLab. The difference between the original intensity of Cy3-probe and the intensity after hybridizing with RCAP can be used to represent the quantity of aptamer produced within a determined time Figure 13 E. The intensity of initial Cy3-probe (i.e., at 0 min) was labeled as $I_0$, while the intensities of Cy3-probe after $t$ min was labeled as $I_t$. The change in relative fluorescence intensity (i.e., consumption of Cy3-probe) can be calculated as $I_0 - I_t$, and the results were plotted against the reaction times, shown in Figure 13 F.

As the results shown, the amplification rate is significantly impaired as the length of inserted polyA increases from 0 to 10 nt, while this amplification rate stays roughly constant when the length of polyA further increases to 15 nt. In the following sections, both the morphology comparison and the capturing performance comparison among RCAPs with different lengths of spacer should be based on a fixed number of aptamers. While simply terminating RCA reactions at the same time point for four different circular probe templates is impractical due to this large amplification rate bias (estimated ~5.5-times amplification rate bias between our fastest and

slowest circular probe templates). Therefore, individually customized RCA reaction times for each template design were calculated based on linear regression curves generated from Figure 13 F. For verification, RCA reactions were conducted at pre-determined time points with corresponding circular probe templates. After incubating with the Cy3-probes (the concentrations of the Cys-probes were controlled constant across four circular probe templates), the Δ relative fluorescent intensities of Cy3-probes were calculated (Figure S2). One-way ANOVA test shows no significant difference between the four different sequences (ns, $p > 0.05$), which confirms the reaction time points chosen for all circular probe templates are reasonably accurate.

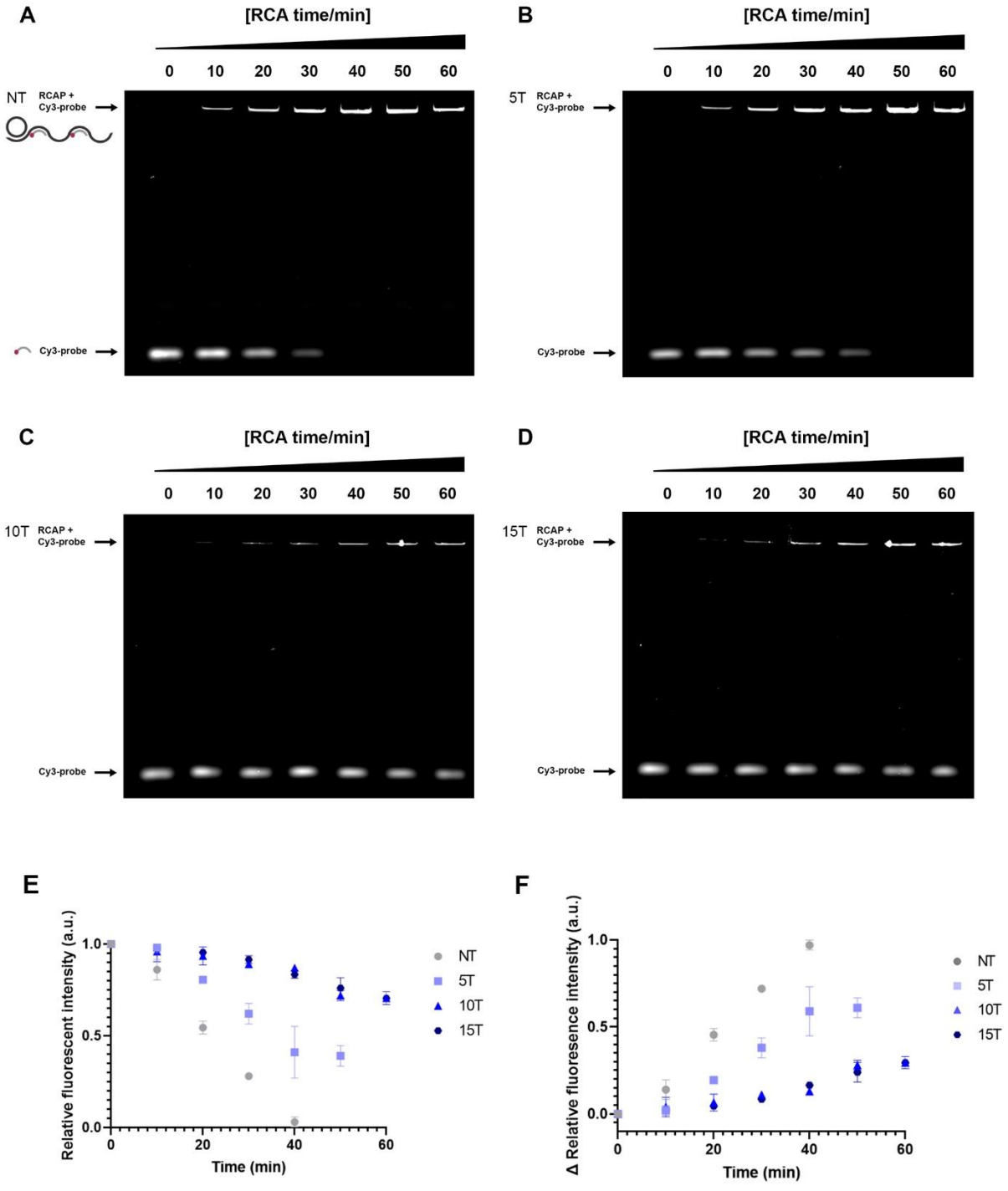
A
[RCA time/min]
0 10 20 30 40 50 60
NT
RCAP +
Cy3-probe
Cy3-probe
B
[RCA time/min]
0 10 20 30 40 50 60
5T
RCAP +
Cy3-probe
Cy3-probe
C
[RCA time/min]
0 10 20 30 40 50 60
10T
RCAP +
Cy3-probe
Cy3-probe
D
[RCA time/min]
0 10 20 30 40 50 60
15T
RCAP +
Cy3-probe
Cy3-probe
E
Relative fluorescent intensity (a.u.)
1.0
0.5
0.0
0 20 40 60
Time (min)
NT
5T
10T
15T
F
Δ Relative fluoresence intensity (a.u.)
1.0
0.5
0.0
0 20 40 60
Time (min)
NT
5T
10T
15T

Figure 13. (A) – (D) Probing the length of amplified product using circular probe template NT (A), 5T (B), 10T (C), and 15T (D) using a fluorescent probe gel shift assay. The secondary structures of RCAP were opened up by heat treatment, followed by mixing with a Cy3-labeled complementary probe. The resultant products were resolved by 8% native PAGE. The gels were imaged under the Cy3 fluorescence channel. The fluorescence intensities of the Cy3-probe bands were used to calculate the linear regression equation for each circular probe template. The same samples without adding Cy3-probe were also resolved using SYBR Gold-stained gel to confirm the production of long ssDNA (Figure S1). (E) and (F) Quantification of RCA amplification rate using Cy3-probe and gel shift assay. Error bars show standard deviations of the measurements (n=2). (A) A plot of relative fluorescence intensities against reaction times. We normalized the unit of relative fluorescent intensity to 1 to represent $I_0$. (B) A plot of changes in relative fluorescence intensity (Δ relative fluorescence intensity) against reaction times. Assuming one unit in Δ relative fluorescence intensity change represents the complete up-shifting of a fixed amount of free Cy3-probes (the number of circular probe template : Cy3-probe= 1: 500).

### 4.4. Water contact angle

To confirm each layer of surface modifications, the water contact angle of PDMS (before plasma treatment), APTES-treated, PAMAM dendrimer engrafted surfaces, and RCAP-modified surfaces using NT, 5T, 10T, and 15T circular probe templates were tested, as shown in Figure 14. The water contact angle of the PDMS surface was 110.58 ± 3.55◦. After APTES treatment, the water contact angle dropped to 45.17 ± 5.34◦. The successful engraftment of PAMAM showed a further decrease in water contact angle to 11.08 ± 1.98◦. These results are consistent with our previously reported data [57, 138]. According to the result from One-way ANOVA test, the measurements of RCAP-conjugated surfaces do not exhibit template-dependent difference (p-value = 0.3460, ns). These data also align with our previously reported result [138] by measuring RCAP-modified surfaces using a different circular probe template, which demonstrates that the water contact angles of RCAP-modified surfaces are not sequence-specific.

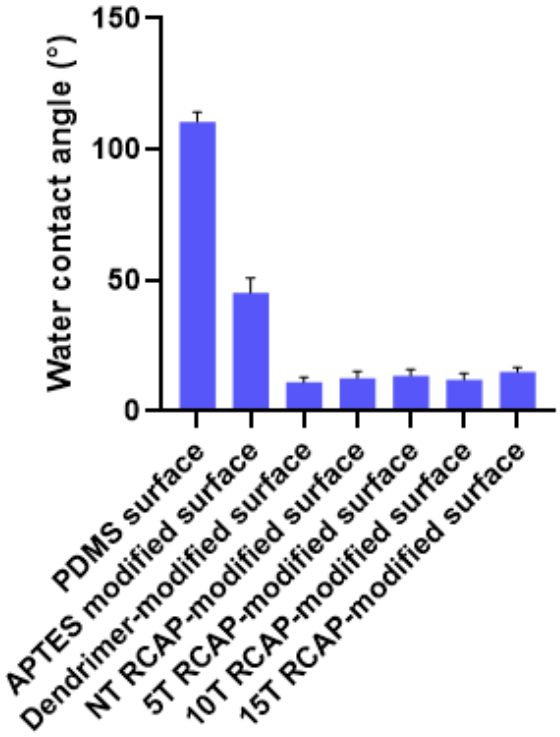


Figure 14. Water contact angles of surfaces with different steps of modifications. Error bars show standard deviations of the measurements (n=3).

### 4.5. Fluorescence probe hybridization assay on RCAP-modified PDMS surface

To further confirm the successful modification of RCAP on the PDMS surface, *in situ* RCA was performed onto the PDMS surface using NT, 5T, 10T, and 15T circular probe templates. Afterwards, Cy3-probes were added directly to the surface without opening the secondary structures. For each experiment, the concentration of circular probe template was controlled at 0.5 μM, and all reactions were terminated at pre-determined time points to generate a fixed number of aptamers. As shown in Figure 15, all RCAP-modified PDMS surfaces showed higher relative fluorescence intensities than the control surface, which proves the successful progression

of *in situ* RCA and the generation of multiple aptamers. Significant differences were revealed among NT, 5T, 10T, and 15T RCAP-modified surfaces. Moreover, 10T and 15T RCAP-modified surfaces showed significantly higher surface fluorescence intensities compared to NT (**, $p \leq 0.01$, and *, $p \leq 0.05$, respectively, unpaired t-test). One reasonable hypothesis is that this difference in surface fluorescence intensities is due to the morphology change of conjugated RCAPs which are discussed in Section 4.7 and 4.8.

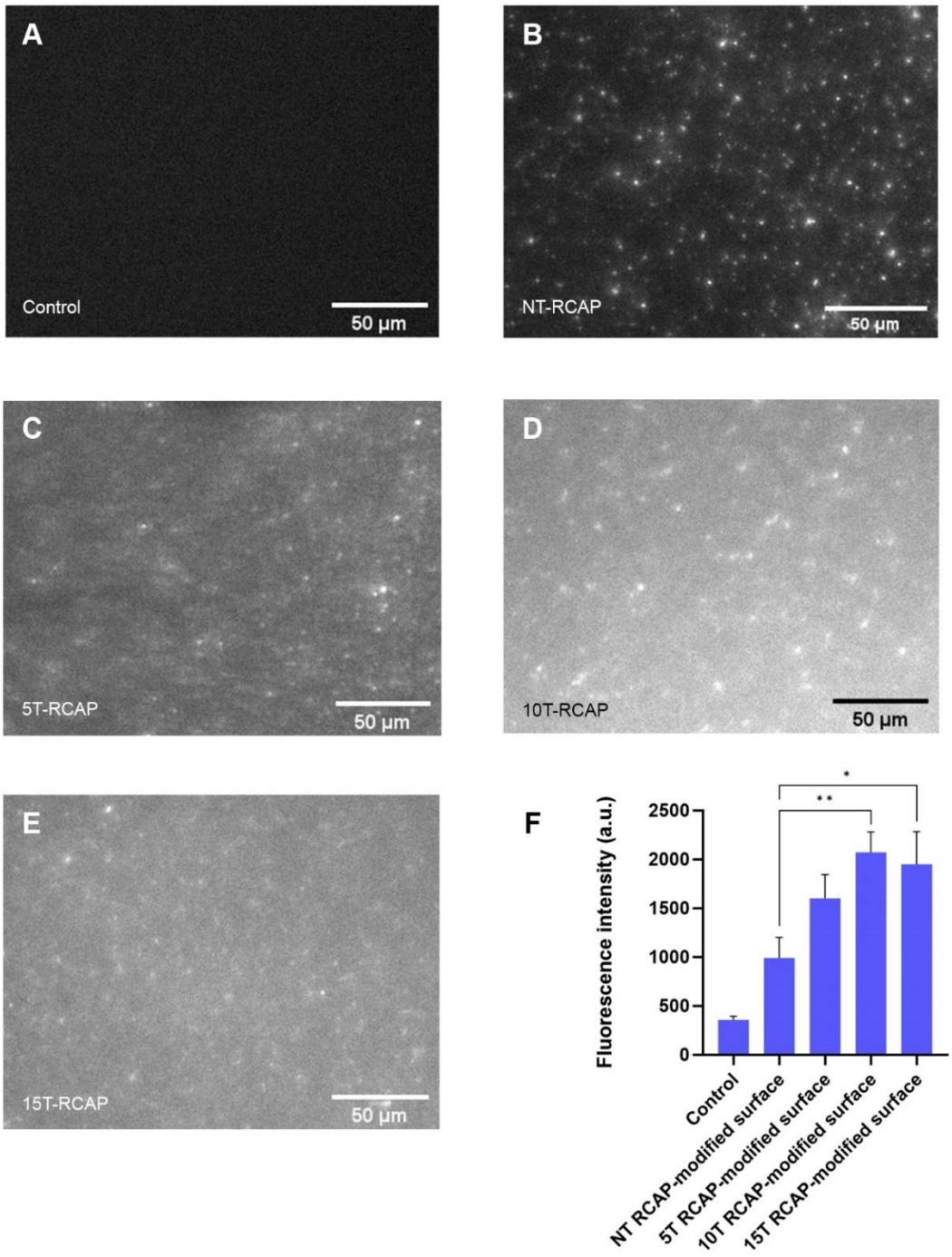


Figure 15. Relative fluorescence intensities of PDMS surfaces modified with NT, 5T, 10T, and 15T RCAP after hybridizing with Cy3-probes. A to E show the fluorescence images of (A) PAMAM dendrimer + primer modified surface; (B) NT RCAP-modified surface; (C) 5T RCAP-modified surface; (D) 10T RCAP-modified surface; (E)

15T RCAP-modified surface. Scale bar = 100 μm. (F) A plot of data from all investigated surfaces. Error bars represent the standard deviations (n = 3).

### 4.6. Microchannel capturing performance and specificity

The capturing performance of RCAP-modified microchannels with different spacer lengths were tested by injecting $10^5$ cells/mL of *E. coli* O157:H7 spiked PBS solution with a flow rate of 0.05 mL/h. As shown in Figure 16 A, PAMAM dendrimer-modified microchannel (i.e., without RCAP) showed almost no cell adhered, which proves the excellent anti-fouling property of the PAMAM dendrimer. Significant differences in captured cell number among four RCAP-modified microchannels were observed (p-value = 0.0010, One-way ANOVA). NT-RCAP modified microchannels showed almost no cells captured (Figure 16 B). For 5T RCAP-modified microchannels, the captured cell numbers slightly increased to 245± 86 (Figure 16 C). 10T RCAP-modified microchannels (Figure 16 D) captured significantly more target cells (1994 ± 140) compared to NT RCAP-modified microchannels. However, increasing the spacer length to 15T seemed to have no more gain: the number of captured cells on 15T RCAP-modified microchannels (1770 ± 294, Figure 16 E) was even slightly less than 10T RCAP-modified microchannels (ns, $p > 0.05$, t-test), but still significantly higher than those of NT and 5T (****, $p \leq 0.0001$, t-test). The above-mentioned results were summarized in Figure 16 G.

In addition, the specificity of cell capture was also tested by injecting $10^5$ cells/mL of nontarget *E.Coli* ATCC25922 cells into the 10T RCAP-modified microchannel. As shown in Figure 16 F and H, nearly no non-target cell was captured in 10T RCAP-modified microchannels, which strongly suggests the specific interaction between RCA-generated aptamers and *E. coli* O157:H7.

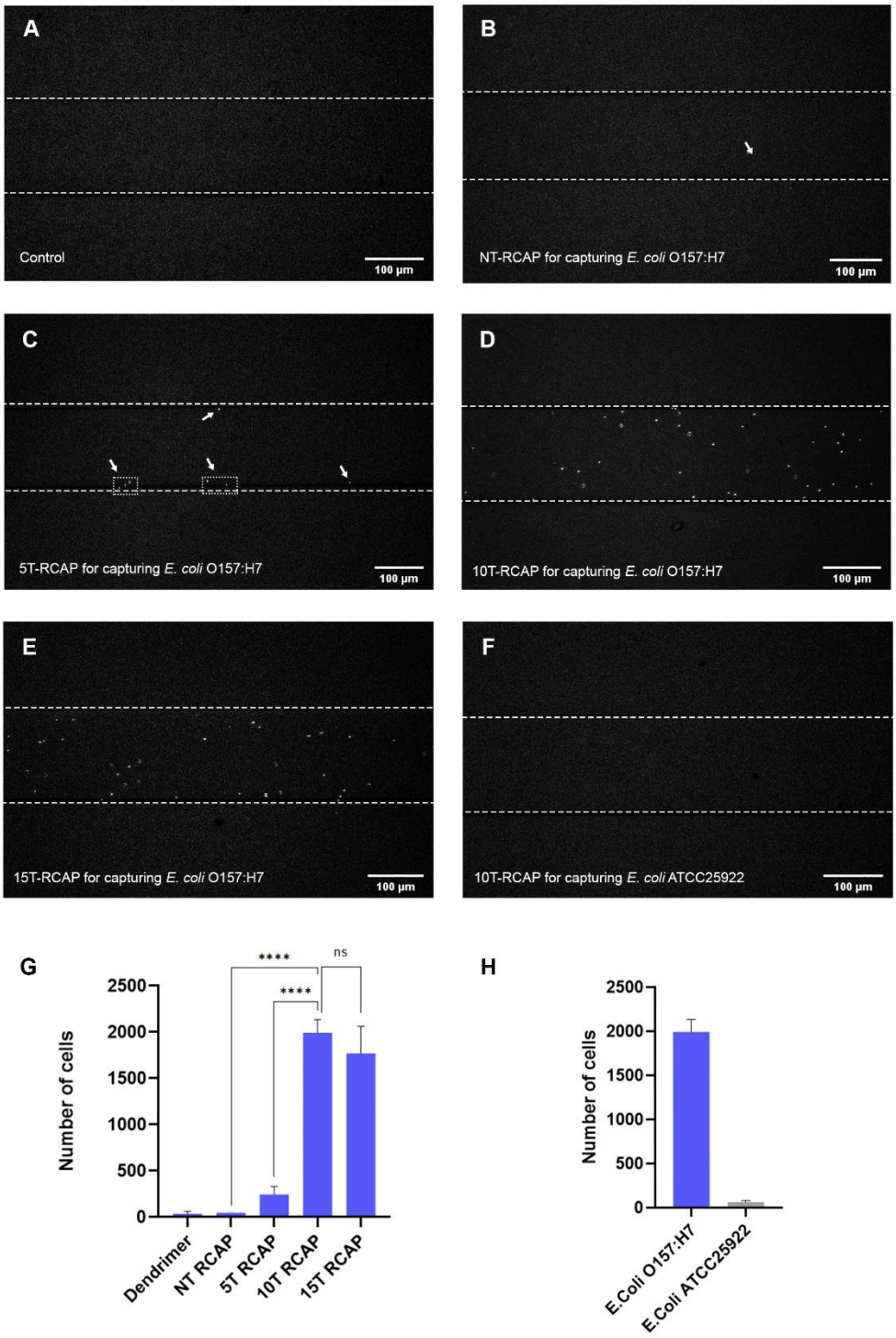


Figure 16. Target cell capturing performances of microchannels modified with different RCAP. A to F show the capturing performances of E. coli O157:H7 in microchannels using (A) dendrimer-engrafted surface, (B) NT RCAP-

dendrimer-modified surface, (C) 5T RCAP-dendrimer-modified surface, (D) 10T RCAP-dendrimer-modified surface, (E) 15T RCAP-dendrimer modified surface. (F) The capturing performances of 10T RCAP-dendrimer-modified microchannel after injecting nontarget E.Coli ATCC25922. (G) The number of captured cells. The significant levels were indicated as following: "****" means $p < 0.0001$; "ns" means $p>0.05$, not significant. Error bars are standard deviations of the measurement (n = 3). (H) The capture specificity was shown by the difference in captured cell numbers using 10T RCAP-modified microchannels after injecting target E. coli O157:H7 and nontarget E.Coli ATCC25922 (n = 3).

### 4.7. Dynamic light scattering of RCAP-conjugated PAMAM dendrimer

It has been suggested that the insertion of spacer between aptamer domains improves the function of multivalent aptamer chains likely by extending the RCAP and increasing the accessibility of aptamer capture motifs [6]. Likewise, we hypothesized that this structural extension can be observed by the difference in the hydrodynamic size ($D_h$) of RCAP-conjugated dendrimer in solution. In brief, the $D_h$ of the RCAP-conjugated dendrimers using NT, 5T, 10T, and 15T templates were measured by DLS. As shown in Figure 17, after conjugating with primer/circular probe template, the $D_h$ of dendrimer increased slightly from 9.97 ± 0.07 nm to 13.13 ± 0.73 nm. After *in situ* RCA reaction, the $D_h$ of all RCAP-conjugated dendrimers greatly increased. One-way ANOVA test demonstrates significant difference(s) exist between four RCAP-conjugated dendrimers. With the number of amplified aptamers controlled in four RCAPs, the order of the sizes was: NT (239.3 ± 11.72 nm) < 5T (581.6 ± 42.48 nm) < 10T (723.7 ± 72.35 nm) ≈ 15T (722.1 ± 27.92 nm), as shown in Figure 17. The $D_h$ of pure RCAP was also tested, and a similar trend was observed (Figure S3). NT and 5T RCAP-conjugated dendrimers showed smaller sizes likely because of their lack of appropriate spacing elements, which leads to inefficient structural support. 10T and 15T RCAP-conjugated dendrimer showed a significantly larger size compared with NT ($p \leq 0.001$ and $p \leq 0.0001$, respectively, unpaired t-test).

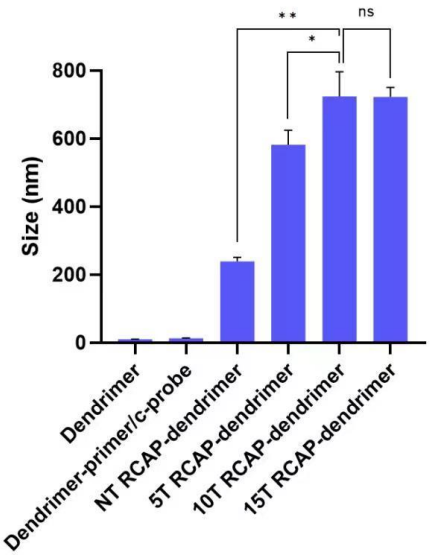


Figure 17. DLS analysis showing hydrodynamic sizes ($D_h$) of the RCAP-conjugated dendrimers. The average $D_h$ of pure dendrimer (control), dendrimer conjugated with primer/circular probe template (10T, control), and NT, 5T, 10T, and 15T RCAP-conjugated dendrimers. All samples were each compared with "10T RCAP-dendrimer", the resulting significant levels were indicated as following: "ns" means $p>0.05$, not significant; "*" means $p < 0.05$; "**" means $p<0.01$, not significant. Error bars represent the standard deviations ($n = 3$).

### 4.8. Testing the level of secondary structures in RCAP

The presence of nonspecific structure has been shown to negatively affect the capturing performance of RCA-generated multivalent aptamer [138, 139]. Therefore, the levels of secondary structures of four different RCAPs were tested and compared. Given that the initial concentration of the circular probe templates and the number of amplification folds were controlled constant, RCAPs generated by NT, 5T, 10T, and 15T were stained with EtBr, a DNA intercalator that is used to characterize the secondary structure of ssDNA [153, 154]. EtBr selectively binds to DNA duplex, while it only weakly binds to the DNA backbone due to the positive charges of EtBr and negative charges of DNA backbone under extreme situations (*e.g.*, when the base-pair duplex binding site are nearly saturated, with at least two orders of magnitude

less in the binding constants) [155]. The fluorescence intensities of the resultant samples were measured in 96-well plates using Synergy H1 microplate reader (BioTek Winooski, Vermont). The acquired data were processed by Gen5 Software V3.09.07 (Bio-Tek, Winooski, VT). As a control, the fluorescence intensities of RCAP samples without EtBr stain were also measured to ensure there is no signal interference caused by autofluorescence of the samples. The results are shown in Figure 18.

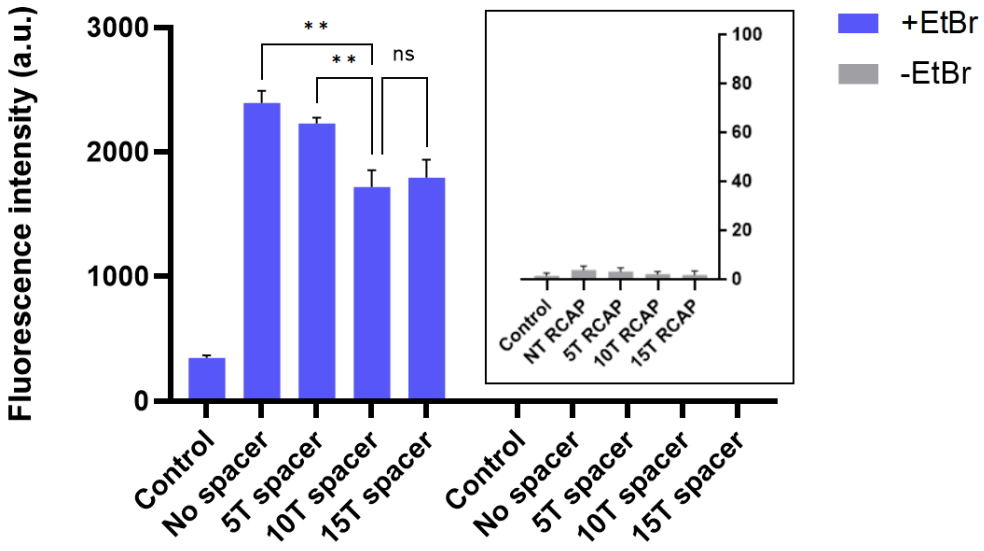


Figure 18. A plot of average fluorescence intensities of RCAPs. The blue bar chart (left) shows the fluorescence intensities after stained with EtBr. The grey bar chart (right) shows the fluorescence intensity without EtBr. The resulting significant levels were indicated as following: "ns" means $p>0.05$, no significant; "**" means $p<0.01$. Error bars represent the standard deviations (n = 3).

Among the four different RCAP samples, NT RCAP shows the highest level of secondary structures. 5T RCAP shows no significant change in fluorescence intensity compared with NT (ns, $p > 0.05$, unpaired t-test). With 10T and 15T RCAP, the change of fluorescence intensity became significant (**, $p \leq 0.005$, unpaired t-test).

Together with the results in Sections 4.6 and 4.7, it can be concluded that covalently connecting multiple aptamers without spacer may lead to the formation of densely compacted RCAP chains that limits the accessibility and disruption of capture motif by forming nonspecific secondary structures. Short spacer (i.e., 5T) captured fewer target cells in microchannels (Figure 16) and does not offer sufficient structural support, which was demonstrated by a smaller RCAP-conjugated dendrimer size (Figure 17) and a higher level of secondary structures in RCAP (Figure 18). In contrast, the incorporation of an appropriate polyT spacer (i.e., 10T or 15T) can mitigate these issues and thus enhance the capturing performance of RCAP. As the length of the spacer reaches 10T or beyond, the size of the RCAP-conjugated dendrimer was enlarged, the level of secondary structure was reduced, and the capturing performances were largely enhanced. In addition, we found that 10T and 15T RCAP have similar hydrodynamic sizes (RCAP-conjugated dendrimers) and levels of secondary structures (Figure 17). This observation may explain the slightly decreased capturing performance of 15T RCAP: within a similar space, the excessive length of the spacer may cause unfavorable conformations such as chain tangles [1, 72], which then slightly impaired the capturing performance of 15T RCAP.

# Chapter 5. Conclusion and Future Work

The effect of various lengths of polyT as intra-molecular spacers in an RCA-generated multivalent aptamer system was investigated. This study was done in three sections: first, to quantify the generated aptamers by investigating the effect of different template designs in aspects of cyclization yield and amplification rate; second, to test the effect of spacer length on the capturing performance of *E.Coli* O157:H7; third, to to characterize the morphology difference in resultant RCAP chains.

The incorporation of polyA (from zero to 15A) into the template linear probe resulted in significantly impaired cyclization yield (from 48% to 14%). This observation can be due to the length difference in linear probes (total length from 72 nt to 87 nt), as the length is agreed to have a large influence on both cyclization yield and amplification rate [120, 150]. Another possible reason is that the polyAs were inserted into the hybridization region of linear probes, which influences the hybridization between linear probes and primers, and subsequently causes less intra-molecular cyclization. For future designs, the location of polyA insertion should also be optimized. Also, we observed a significant amplification rate bias on the four templates. Besides template length, this amplification rate bias can also be caused by different thermal stabilities ($T_m$) of the primer-circular probe template duplexes [157]. We didn't observe the similar sinusoidal amplification rate bias with respect to circular probe template length, as discovered by Joffory's group [150]. The contrary can be caused by the difference in the hybridization zone of circular probe templates or the probe length interval we've chosen for this study. Nevertheless, our measured average amplification rate of the templates is similar to results obtained by other groups (≈0.4 kb/min) [158].

We also found that directly connecting aptamer without any spacer can lead to poor capturing performance, demonstrated by almost no cell captured by NT RCAP-dendrimer modified microchannels. The capturing performance was enhanced after incorporating appropriate intra-molecular spacers. Specifically, inserting 10T and 15T spacers can greatly enhance the capturing performance, likely by providing structural support to RCAP and reducing nonspecific secondary structures. The insertion of polyT dramatically increases the hydrodynamic size of RCAP, which agrees other groups' results [142, 143]. Such a structural extension has been suggested enhance the capturing performance of multivalent aptamer chains [6]. In addition, the secondary structure level of RCAP is also significantly reduced after incorporating 10T or longer spacers.

In summary, for the aptamer that we have studied, incorporating longer polyT motifs as an intra-molecular spacer can result in a trade-off between the yield and the capturing performance of the RCAP. For future studies that apply RCA-generated multivalent aptamer design, an optimization step of intra-molecular spacer length is recommended since it may significantly influence the capturing performance of RCAP. On the other hand, in order to maximize the yield of RCAP, the selection of original aptamer is also crucial: we suggest choosing aptamers that lie between 40 to 60 nt in length. As such, an insertion of a 10 nt spacer will make the total length of the linear probe lie between 50 to 70 nt, which can ensure a relatively high yield of the circular probe template.

For future studies, the following topics are suggested:

1. Applying RCA-generated multivalent aptamer chains in microchannels, particularly straight microchannels, is challenging because the long ssDNA chain has to overcome several obstacles,

such as shear stress. A thoughtful design of channel structure and more sophisticated surface modification may be beneficial for overall performance.

2. Heterovalent aptamer design (*i.e.*, using two or more aptamers to target different motif on the same target cell) can also be a potential strategy for improving the performance of the PAMAM dendrimer-modified microfluidic system.

3. Flexible-rigid spacer (dsDNA combined with few bases of ssDNA) with proper length has been suggested to be an ideal intra-molecular spacer. Applying this design to an RCA-generated multivalent system is also an interesting topic to study.

# References


1. Mallikaratchy, P.R., et al., *A multivalent DNA aptamer specific for the B-cell receptor on human lymphoma and leukemia.* Nucleic Acids Res, 2011. **39**(6): p. 2458-69.
2. Kiessling, L. and A. Lamanna, *Multivalency in biological systems*, in *Chemical Probes in Biology*. 2003, Springer. p. 345-357.
3. Keefe, A.D., S. Pai, and A. Ellington, *Aptamers as therapeutics.* Nature Reviews Drug Discovery, 2010. **9**(7): p. 537-550.
4. Wu, Y., et al., *Enhanced targeted gene transduction: AAV2 vectors conjugated to multiple aptamers via reducible disulfide linkages.* Journal of the American Chemical Society, 2018. **140**(1): p. 2-5.
5. Jin, Y., et al., *Biodegradable, multifunctional DNAzyme nanoflowers for enhanced cancer therapy.* NPG Asia Materials, 2017. **9**(3): p. e365-e365.
6. Zhao, W., et al., *Bioinspired multivalent DNA network for capture and release of cells.* Proc Natl Acad Sci U S A, 2012. **109**(48): p. 19626-31.
7. Yang, J., et al., *In Situ-Generated Multivalent Aptamer Network for Efficient Capture and Sensitive Electrochemical Detection of Circulating Tumor Cells in Whole Blood.* Analytical Chemistry, 2020. **92**(11): p. 7893-7899.
8. Kapadia, C.H., J.R. Melamed, and E.S. Day, *Spherical nucleic acid nanoparticles: Therapeutic potential.* BioDrugs, 2018. **32**(4): p. 297-309.
9. Taghdisi, S.M., et al., *Double targeting, controlled release and reversible delivery of daunorubicin to cancer cells by polyvalent aptamers-modified gold nanoparticles.* Materials Science and Engineering: C, 2016. **61**: p. 753-761.
10. Yazdanparast, S., et al., *Dual-aptamer based electrochemical sandwich biosensor for MCF-7 human breast cancer cells using silver nanoparticle labels and a poly (glutamic acid)/MWNT nanocomposite.* Microchimica Acta, 2018. **185**(9): p. 405.
11. Li, J., et al., *On-chip, aptamer-based sandwich assay for detection of glycated hemoglobins via magnetic beads.* Biosensors and Bioelectronics, 2016. **79**: p. 887-893.
12. Zhu, H., et al., *Aptamer-PEG-modified Fe 3 O 4@ Mn as a novel T1-and T2-dual-model MRI contrast agent targeting hypoxia-induced cancer stem cells.* Scientific reports, 2016. **6**(1): p. 1-12.
13. Chen, Y., et al., *Regenerative NanoOctopus Based on Multivalent-Aptamer-Functionalized Magnetic Microparticles for Effective Cell Capture in Whole Blood.* Analytical Chemistry, 2019. **91**(6): p. 4017-4022.
14. Wang, X., et al., *Aggregation-induced emission luminogen-embedded silica nanoparticles containing DNA aptamers for targeted cell imaging.* ACS applied materials & interfaces, 2016. **8**(1): p. 609-616.
15. Yang, Y., et al., *An efficient cell-targeting drug delivery system based on aptamer-modified mesoporous silica nanoparticles.* 2019. **14**(1): p. 1-10.
16. Taghavi, S., et al., *Chitosan-modified PLGA nanoparticles tagged with 5TR1 aptamer for in vivo tumor-targeted drug delivery.* Cancer Letters, 2017. **400**: p. 1-8.

17. Zhang, J., et al., *Simply-Self-Assembled Targeting DNA Nano-Sea-urchin as Multivalent Drug Carrier.* ACS Applied Bio Materials, 2020.
18. Novoselov, K.S., et al., *Electric field effect in atomically thin carbon films.* 2004. **306**(5696): p. 666-669.
19. Yang, L., et al., *Photothermal therapeutic response of cancer cells to aptamer-gold nanoparticle-hybridized graphene oxide under NIR illumination.* ACS Appl Mater Interfaces, 2015. **7**(9): p. 5097-106.
20. Zhao, L., et al., *A fluorescent biosensor based on molybdenum disulfide nanosheets and protein aptamer for sensitive detection of carcinoembryonic antigen.* Sensors and Actuators B: Chemical, 2018. **273**: p. 185-190.
21. Chen, L., et al., *Biodegradable mesoporous organosilica nanosheets for chemotherapy/mild thermotherapy of cancer: Fast internalization, high cellular uptake, and high drug loading.* 2020. **12**(27): p. 30234-30246.
22. Peng, L., et al., *Monolayer nanosheets with an extremely high drug loading toward controlled delivery and cancer theranostics.* 2018. **30**(16): p. 1707389.
23. Pan, Q., et al., *Aptamer-Functionalized DNA Origami for Targeted Codelivery of Antisense Oligonucleotides and Doxorubicin to Enhance Therapy in Drug-Resistant Cancer Cells.* ACS Appl Mater Interfaces, 2020. **12**(1): p. 400-409.
24. Sun, P., et al., *Site-specific anchoring aptamer C2NP on DNA origami nanostructures for cancer treatment.* RSC Advances, 2018. **8**(46): p. 26300-26308.
25. Mela, I., et al., *DNA Nanostructures for Targeted Antimicrobial Delivery.* Angew Chem Int Ed Engl, 2020. **59**(31): p. 12698-12702.
26. Zhao, S., et al., *Efficient intracellular delivery of RNase A using DNA origami carriers.* 2019. **11**(12): p. 11112-11118.
27. Tintoré, M., et al., *DNA Origami as a DNA Repair Nanosensor at the Single-Molecule Level.* 2013. **125**(30): p. 7901-7904.
28. Godonoga, M., et al., *A DNA aptamer recognising a malaria protein biomarker can function as part of a DNA origami assembly.* Sci Rep, 2016. **6**: p. 21266.
29. Liu, Y., et al., *Highly Sensitive Minimal Residual Disease Detection by Biomimetic Multivalent Aptamer Nanoclimber Functionalized Microfluidic Chip.* Small, 2020. **16**(20): p. 2000949.
30. Gao, M.-L., B.-C. Yin, and B.-C. Ye, *Construction of a DNA-AuNP-based satellite network for exosome analysis.* Analyst, 2019. **144**(20): p. 5996-6003.
31. Jeong, H., et al., *Multivalent Aptamer–RNA Conjugates for Simple and Efficient Delivery of Doxorubicin/siRNA into Multidrug-Resistant Cells.* Macromolecular bioscience, 2017. **17**(4): p. 1600343.
32. Yazdian-Robati, R., et al., *Targeted Delivery of Epirubicin to Cancer Cells by Polyvalent Aptamer System in vitro and in vivo.* Pharm Res, 2016. **33**(9): p. 2289-97.
33. Xue, C., et al., *Periodically Ordered, Nuclease-Resistant DNA Nanowires Decorated with Cell-Specific Aptamers as Selective Theranostic Agents.* Angew Chem Int Ed Engl, 2020.
34. Rutten, I., D. Daems, and J.J.J.o.M.C.B. Lammertyn, *Boosting biomolecular interactions through DNA origami nano-tailored biosensing interfaces.* 2020. **8**(16): p. 3606-3615.
35. Li, S., et al., *A DNA nanorobot functions as a cancer therapeutic in response to a molecular trigger in vivo.* Nat Biotechnol, 2018. **36**(3): p. 258-264.

36. Chang, E.K., et al., *Facile supermolecular aptamer inhibitors of L-selectin.* PLoS One, 2015. **10**(3): p. e0123034.
37. Song, Y., et al., *Bioinspired Engineering of a Multivalent Aptamer-Functionalized Nanointerface to Enhance the Capture and Release of Circulating Tumor Cells.* Angewandte Chemie International Edition, 2019. **58**(8): p. 2236-2240.
38. Zhang, Z., et al., *A polyvalent aptamer system for targeted drug delivery.* 2013. **34**(37): p. 9728-9735.
39. Li, W., et al., *Self-assembled DNA nanocentipede as multivalent drug carrier for targeted delivery.* ACS applied materials & interfaces, 2016. **8**(39): p. 25733-25740.
40. Jolly, P., et al., *Aptamer–MIP hybrid receptor for highly sensitive electrochemical detection of prostate specific antigen.* 2016. **75**: p. 188-195.
41. Liu, X., et al., *Novel hybrid probe based on double recognition of aptamer-molecularly imprinted polymer grafted on upconversion nanoparticles for enrofloxacin sensing.* 2017. **87**: p. 203-208.
42. Zhang, Z., J.J.A.a.m. Liu, and interfaces, *Molecularly imprinted polymers with DNA aptamer fragments as macromonomers.* 2016. **8**(10): p. 6371-6378.
43. Liu, L., et al., *Artificial antibody with site-enhanced multivalent aptamers for specific capture of circulating tumor cells.* Analytical chemistry, 2019. **91**(4): p. 2591-2594.
44. Tang, M.S., et al., *An aptamer-enabled DNA nanobox for protein sensing.* 2018. **14**(4): p. 1161-1168.
45. Liu, K., C. Xu, and J. Liu, *Regulation of cell binding and entry by DNA origami mediated spatial distribution of aptamers.* J Mater Chem B, 2020. **8**(31): p. 6802-6809.
46. Han, X., et al., *Multivalent aptamer-modified tetrahedral DNA nanocage demonstrates high selectivity and safety for anti-tumor therapy.* 2019. **11**(1): p. 339-347.
47. Li, Q., et al., *Aptamer-modified tetrahedral DNA nanostructure for tumor-targeted drug delivery.* 2017. **9**(42): p. 36695-36701.
48. Lu, Z., et al., *Aptamer-tagged DNA origami for spatially addressable detection of aflatoxin B1.* 2017. **53**(5): p. 941-944.
49. Cao, M., et al., *Multivalent Aptamer-modified DNA Origami as Drug Delivery System for Targeted Cancer Therapy.* Chemical Research in Chinese Universities, 2019: p. 1-7.
50. Zhang, P., et al., *Aptamer-coded DNA nanoparticles for targeted doxorubicin delivery using pH-sensitive spacer.* Frontiers of Chemical Science and Engineering, 2017. **11**(4): p. 529-536.
51. Lao, Y.-H., K. Peck, and L.-C. Chen, *Enhancement of Aptamer Microarray Sensitivity through Spacer Optimization and Avidity Effect.* Analytical Chemistry, 2009. **81**(5): p. 1747-1754.
52. Mahlknecht, G., et al., *Multimerization of ERBB2/HER2 specific aptamer leads to improved receptor binding.* Biochem Biophys Res Commun, 2015. **465**(2): p. 218-24.
53. Hayat, A., et al., *Design of PEG-aptamer two piece macromolecules as convenient and integrated sensing platform: Application to the label free detection of small size molecules.* 2013. **45**: p. 168-173.
54. Waybrant, B., T.R. Pearce, and E. Kokkoli, *Effect of Polyethylene Glycol, Alkyl, and Oligonucleotide Spacers on the Binding, Secondary Structure, and Self-Assembly of Fractalkine Binding FKN-S2 Aptamer-Amphiphiles.* Langmuir, 2014. **30**(25): p. 7465-7474.
55. Kuang, H., et al., *Effect of an alkyl spacer on the morphology and internalization of MUC1 aptamer-naphthalimide amphiphiles for targeting and imaging triple negative breast cancer cells.* 2021. **6**(1): p. e10194.

56. Chen, N., et al., *Cell adhesion on an artificial extracellular matrix using aptamer-functionalized PEG hydrogels.* Biomaterials, 2012. **33**(5): p. 1353-1362.
57. Qin, Y., et al., *Target capturing performance of microfluidic channel surface immobilized aptamers: the effects of spacer lengths.* Biomed Microdevices, 2019. **21**(3): p. 54.
58. Ueno, Y., et al., *On-chip FRET graphene oxide aptasensor: quantitative evaluation of enhanced sensitivity by aptamer with a double-stranded DNA spacer.* 2015. **31**(9): p. 875-879.
59. Xing, H., et al., *The Effects of Spacer Length and Composition on Aptamer-Mediated Cell-Specific Targeting with Nanoscale PEGylated Liposomal Doxorubicin.* Chembiochem, 2016. **17**(12): p. 1111-7.
60. Goda, T., et al., *Dual aptamer-immobilized surfaces for improved affinity through multiple target binding in potentiometric thrombin biosensing.* 2015. **73**: p. 174-180.
61. Zhu, G., et al., *Characterization of Optimal Aptamer-Microarray Binding Chemistry and Spacer Design.* Chemical Engineering & Technology, 2011. **34**(12): p. 2022-2028.
62. Balamurugan, S., et al., *Effect of linker structure on surface density of aptamer monolayers and their corresponding protein binding efficiency.* 2008. **80**(24): p. 9630-9634.
63. Edwards, K.A., A.J.J.A. Baeumner, and b. chemistry, *Aptamer sandwich assays: label-free and fluorescence investigations of heterogeneous binding events.* 2010. **398**(6): p. 2635-2644.
64. Kim, Y.S., et al., *Aptamer cocktails: enhancement of sensing signals compared to single use of aptamers for detection of bacteria.* Biosens Bioelectron, 2014. **54**: p. 195-8.
65. Lin, Y., et al., *DNA-mediated reversible capture and release of circulating tumor cells with a multivalent dual-specific aptamer coating network.* Chemical Communications, 2019. **55**(37): p. 5387-5390.
66. Brouwer, A., et al., *Evaluation and consequences of heterogeneity in the circulating tumor cell compartment.* 2016. **7**(30): p. 48625.
67. Qin, W., et al., *Bioinspired DNA nanointerface with anisotropic aptamers for accurate capture of circulating tumor cells.* 2020. **7**(19): p. 2000647.
68. Zhao, L., et al., *Enhanced and Differential Capture of Circulating Tumor Cells from Lung Cancer Patients by Microfluidic Assays Using Aptamer Cocktail.* Small, 2016. **12**(8): p. 1072-81.
69. Dou, B., et al., *Aptamer-Functionalized and Gold Nanoparticle Array-Decorated Magnetic Graphene Nanosheets Enable Multiplexed and Sensitive Electrochemical Detection of Rare Circulating Tumor Cells in Whole Blood.* Anal Chem, 2019. **91**(16): p. 10792-10799.
70. Dai, Z., et al., *A highly versatile platform based on geometrically well-defined 3D DNA nanostructures for selective recognition and positioning of multiplex targets.* Nanoscale, 2016. **8**(43): p. 18291-18295.
71. Kwon, P.S., et al., *Designer DNA architecture offers precise and multivalent spatial pattern-recognition for viral sensing and inhibition.* Nat Chem, 2020. **12**(1): p. 26-35.
72. Zhao, X., J.T. Lis, and H.J.N.a.t. Shi, *A systematic study of the features critical for designing a high avidity multivalent aptamer.* 2013. **23**(3): p. 238-242.
73. Zhao, X., J.T. Lis, and H. Shi, *A systematic study of the features critical for designing a high avidity multivalent aptamer.* Nucleic acid therapeutics, 2013. **23**(3): p. 238-242.
74. Hasegawa, H., et al., *Improvement of aptamer affinity by dimerization.* 2008. **8**(2): p. 1090-1098.
75. Aghebat Rafat, A., et al., *Barcoded DNA origami structures for multiplexed optimization and enrichment of DNA-based protein-binding cavities.* Nat Chem, 2020. **12**(9): p. 852-859.

76. Santulli-Marotto, S., et al., *Multivalent RNA aptamers that inhibit CTLA-4 and enhance tumor immunity.* 2003. **63**(21): p. 7483-7489.
77. Krissanaprasit, A., et al., *Multivalent Aptamer-Functionalized Single-Strand RNA Origami as Effective, Target-Specific Anticoagulants with Corresponding Reversal Agents.* 2021. **10**(11): p. 2001826.
78. Rinker, S., et al., *Self-assembled DNA nanostructures for distance-dependent multivalent ligand–protein binding.* 2008. **3**(7): p. 418-422.
79. Bujotzek, A., et al., *Towards a rational spacer design for bivalent inhibition of estrogen receptor.* J Comput Aided Mol Des, 2011. **25**(3): p. 253-62.
80. Chen, Y., et al., *Non-invasive isolation of rare circulating tumor cells with a DNA mimic of double-sided tape using multimeric aptamers.* Nanoscale, 2019. **11**(13): p. 5879-5883.
81. Ding, C., et al., *Multivalent Aptamer Functionalized Ag2S Nanodots/Hybrid Cell Membrane-Coated Magnetic Nanobioprobe for the Ultrasensitive Isolation and Detection of Circulating Tumor Cells.* Advanced Functional Materials, 2020. **30**(16): p. 1909781.
82. Wu, L., et al., *Fluidic Multivalent Membrane Nanointerface Enables Synergetic Enrichment of Circulating Tumor Cells with High Efficiency and Viability.* J Am Chem Soc, 2020. **142**(10): p. 4800-4806.
83. Jiang, Y., et al., *Developing a dual-RCA microfluidic platform for sensitive E. coli O157:H7 whole-cell detections.* Analytica Chimica Acta, 2020. **1127**: p. 79-88.
84. Hao, X., et al., *Aptamer surface functionalization of microfluidic devices using dendrimers as multi-handled templates and its application in sensitive detections of foodborne pathogenic bacteria.* 2019. **1056**: p. 96-107.
85. Jiang, Y., S. Zou, and X. Cao, *A simple dendrimer-aptamer based microfluidic platform for E. coli O157:H7 detection and signal intensification by rolling circle amplification.* Sensors and Actuators B: Chemical, 2017. **251**: p. 976-984.
86. Xue, F., et al., *Isolation of extracellular vesicles with multivalent aptamers.* 2021. **146**(1): p. 253-261.
87. Huang, Y., et al., *An aptamer cocktail-based electrochemical aptasensor for direct capture and rapid detection of tetracycline in honey.* Microchemical Journal, 2019. **150**.
88. Zhu, J., et al., *Specific capture and temperature-mediated release of cells in an aptamer-based microfluidic device.* Lab on a chip, 2012. **12**(18): p. 3504-3513.
89. Zhang, Z., et al., *Programmable hydrogels for controlled cell catch and release using hybridized aptamers and complementary sequences.* Journal of the American Chemical Society, 2012. **134**(38): p. 15716-15719.
90. Bian, Q., et al., *Light-triggered specific cancer cell release from cyclodextrin/azobenzene and aptamer-modified substrate.* ACS Applied Materials & Interfaces, 2016. **8**(40): p. 27360-27367.
91. Sheng, W., et al., *Multivalent DNA nanospheres for enhanced capture of cancer cells in microfluidic devices.* 2013. **7**(8): p. 7067-7076.
92. Chen, J., et al., *A novel method combining aptamer-Ag10NPs based microfluidic biochip with bright field imaging for detection of KPC-2-expressing bacteria.* Anal Chim Acta, 2020. **1132**: p. 20-27.
93. Qin, Y., et al., *Developing an ultra non-fouling SU-8 and PDMS hybrid microfluidic device by poly (amidoamine) engraftment.* 2015. **127**: p. 247-255.

94. Guan, B. and X.J.I.j.o.n. Zhang, *Aptamers as versatile ligands for biomedical and pharmaceutical applications.* 2020. **15**: p. 1059.
95. Cao, Z., X. Zhou, and G. Wang, *Selective release of hydrophobic and hydrophilic cargos from multi-stimuli-responsive nanogels.* ACS applied materials & interfaces, 2016. **8**(42): p. 28888-28896.
96. Wang, J., et al., *Nonviolent self-catabolic DNAzyme nanosponges for smart anticancer drug delivery.* ACS nano, 2019. **13**(5): p. 5852-5863.
97. Yoo, H., et al., *Multivalent comb-type aptamer–siRNA conjugates for efficient and selective intracellular delivery.* 2014. **50**(51): p. 6765-6767.
98. Sun, W., et al., *Self-assembled DNA nanoclews for the efficient delivery of CRISPR–Cas9 for genome editing.* Angewandte Chemie, 2015. **127**(41): p. 12197-12201.
99. Shi, J., et al., *MicroRNA-responsive release of Cas9/sgRNA from DNA nanoflower for cytosolic protein delivery and enhanced genome editing.* 2020. **256**: p. 120221.
100. Sathiyaseelan, A., et al., *pH-controlled nucleolin targeted release of dual drug from chitosan-gold based aptamer functionalized nano drug delivery system for improved glioblastoma treatment.* 2021. **262**: p. 117907.
101. Charbgoo, F., et al., *MUC1 aptamer-targeted DNA micelles for dual tumor therapy using doxorubicin and KLA peptide.* 2018. **14**(3): p. 685-697.
102. Zhu, Y.-J., et al., *Stable, polyvalent aptamer-conjugated near-infrared fluorescent nanocomposite for high-performance cancer cell-targeted imaging and therapy.* Journal of Materials Chemistry B, 2017. **5**(46): p. 9229-9237.
103. Pascual, L., et al., *MUC1 aptamer-capped mesoporous silica nanoparticles for controlled drug delivery and radio-imaging applications.* 2017. **13**(8): p. 2495-2505.
104. Kratschmer, C. and M.J.N.a.t. Levy, *Effect of chemical modifications on aptamer stability in serum.* 2017. **27**(6): p. 335-344.
105. Han, G.-M., et al., *Biostable L-DNA-templated aptamer-silver nanoclusters for cell-type-specific imaging at physiological temperature.* 2016. **88**(22): p. 10800-10804.
106. Hianik, T., et al., *Influence of ionic strength, pH and aptamer configuration for binding affinity to thrombin.* 2007. **70**(1): p. 127-133.
107. Shi, P., et al., *In Situ Synthesis of an Aptamer-Based Polyvalent Antibody Mimic on the Cell Surface for Enhanced Interactions between Immune and Cancer Cells.* Angewandte Chemie International Edition, 2020.
108. Zou, S., et al., *Extracellular pH-manipulated in situ reconfiguration of aptamer functionalized DNA monomer enables specifically improved affinity, detection and drug delivery.* 2020. **145**(7): p. 2562-2569.
109. Li, H., et al., *Aptamer internalization via Endocytosis inducing S-phase arrest and priming Maver-1 lymphoma cells for Cytarabine chemotherapy.* Theranostics, 2017. **7**(5): p. 1204.
110. Banerjee, D., et al., *Multivalent display and receptor-mediated endocytosis of transferrin on virus-like particles.* ChemBioChem, 2010. **11**(9): p. 1273-1279.
111. Kang, Y.Y., et al., *Implication of multivalent aptamers in DNA and DNA–RNA hybrid structures for efficient drug delivery in vitro and in vivo.* Journal of Industrial and Engineering Chemistry, 2018. **60**: p. 250-258.

112. Liu, Z., et al., *Aptamer density dependent cellular uptake of lipid-capped polymer nanoparticles for polyvalent targeted delivery of vinorelbine to cancer cells.* RSC Advances, 2015. **5**(22): p. 16931-16939.
113. Alizadeh, L., et al., *AS1411 aptamer-functionalized chitosan-silica nanoparticles for targeted delivery of epigallocatechin gallate to the SKOV-3 ovarian cancer cell lines.* Journal of Nanoparticle Research, 2020. **22**(1): p. 1-14.
114. Zhao, Z., et al., *Activatable Fluorescence/MRI Bimodal Platform for Tumor Cell Imaging via MnO2 Nanosheet–Aptamer Nanoprobe.* Journal of the American Chemical Society, 2014. **136**(32): p. 11220-11223.
115. Gao, L., et al., *Zinc Ion-Stabilized Aptamer-Targeted Black Phosphorus Nanosheets for Enhanced Photothermal/Chemotherapy Against Prostate Cancer.* Front Bioeng Biotechnol, 2020. **8**: p. 769.
116. Zhang, Z., et al., *Rolling Circle Amplification-Based Polyvalent Molecular Beacon Probe-Assisted Signal Amplification Strategies for Sensitive Detection of B16 Cells.* ACS Biomaterials Science & Engineering, 2020. **6**(5): p. 3114-3121.
117. Tang, J., et al., *Polyvalent and Thermosensitive DNA Nanoensembles for Cancer Cell Detection and Manipulation.* Anal Chem, 2017. **89**(12): p. 6637-6644.
118. Luo, L., et al., *Sensitive and specific detection of tumour cells based on a multivalent DNA nanocreeper and a multiplexed fluorescence supersandwich.* Chemical Communications, 2020. **56**(25): p. 3693-3696.
119. An, R., et al., *Highly efficient preparation of single-stranded DNA rings by T4 ligase at abnormally low Mg(II) concentration.* Nucleic Acids Res, 2017. **45**(15): p. e139.
120. Cui, Y., et al., *Terminal hairpin in oligonucleotide dominantly prioritizes intramolecular cyclization by T4 ligase over intermolecular polymerization: an exclusive methodology for producing ssDNA rings.* 2018. **46**(22): p. e132-e132.
121. Sui, Z., et al., *Efficient Preparation of Large-Sized Rings of Single-Stranded DNA through One-Pot Ligation of Multiple Fragments.* Chem Asian J, 2019. **14**(19): p. 3251-3254.
122. Diegelman, A.M. and E.T.J.C.p.i.n.a.c. Kool, *Chemical and Enzymatic Methods for Preparing Circular Single-Stranded DNAs.* 2000(1): p. 5.2. 1-5.2. 27.
123. Cui, Y., et al., *Cyclization of secondarily structured oligonucleotides to single-stranded rings by using Taq DNA ligase at high temperatures.* RSC Advances, 2018. **8**(34): p. 18972-18979.
124. Sasaki, N., et al., *Molecular crowding improves bead-based padlock rolling circle amplification.* Anal Biochem, 2017. **519**: p. 15-18.
125. Sasaki, N., et al., *Mechanistic investigation of bead-based padlock rolling circle amplification under molecular crowding conditions.* Anal Biochem, 2020. **593**: p. 113596.
126. Dean, F.B., et al., *Rapid amplification of plasmid and phage DNA using Phi 29 DNA polymerase and multiply-primed rolling circle amplification.* Genome Res, 2001. **11**(6): p. 1095-9.
127. Liu, X., et al., *A ternary probe for target-triggered autonomous multi-branch rolling circle amplification for highly sensitive colorimetric sensing of platelet-derived growth factor BB.* 2020. **305**: p. 127405.
128. Cao, A. and C.-y.J.A.c. Zhang, *Sensitive and label-free DNA methylation detection by ligation-mediated hyperbranched rolling circle amplification.* 2012. **84**(14): p. 6199-6205.
129. Dahl, F., et al., *Circle-to-circle amplification for precise and sensitive DNA analysis.* 2004. **101**(13): p. 4548-4553.

130. Murakami, T., J. Sumaoka, and M.J.N.a.r. Komiyama, *Sensitive isothermal detection of nucleic-acid sequence by primer generation–rolling circle amplification.* 2009. **37**(3): p. e19-e19.
131. Zhu, X., et al., *A netlike rolling circle nucleic acid amplification technique.* Analyst, 2015. **140**(1): p. 74-8.
132. Li, D., et al., *Efficient and exponential rolling circle amplification molecular network leads to ultrasensitive and label-free detection of microRNA.* 2019. **92**(2): p. 2074-2079.
133. Xu, H., et al., *Exponential rolling circle amplification and its sensing application for highly sensitive DNA detection of tumor suppressor gene.* 2017. **243**: p. 1240-1247.
134. Zhang, C., et al., *Comparative detection of Karenia mikimotoi by exponential rolling circle amplification (E-RCA) and double-ligation E-RCA.* 2019. **31**(1): p. 505-518.
135. Yue, S., et al., *Rolling circle replication for biosensing, bioimaging, and biomedicine.* 2021.
136. Liu, M., et al., *DNAzyme feedback amplification: relaying molecular recognition to exponential DNA amplification.* 2018. **24**(18): p. 4473-4479.
137. Cai, W., et al., *Immobilized-free miniaturized electrochemical sensing system for Pb2+ detection based on dual Pb2+-DNAzyme assistant feedback amplification strategy.* 2018. **117**: p. 312-318.
138. Li, S., et al., *In situ rolling circle amplification surface modifications to improve E. coli O157:H7 capturing performances for rapid and sensitive microfluidic detection applications.* Anal Chim Acta, 2021. **1150**: p. 338229.
139. Xie, L., et al., *Nanostructural morphology master-regulated the cell capture efficiency of multivalent aptamers.* RSC Advances, 2015. **5**(50): p. 39791-39798.
140. Yang, J., et al., *In situ-generated multivalent aptamer network for efficient capture and sensitive electrochemical detection of circulating tumor cells in whole blood.* 2020. **92**(11): p. 7893-7899.
141. Wang, Z., et al., *Virus-mimicking cell capture using heterovalency magnetic DNA nanoclaws.* 2019. **11**(13): p. 12244-12252.
142. Zhu, G., et al., *Noncanonical self-assembly of multifunctional DNA nanoflowers for biomedical applications.* J Am Chem Soc, 2013. **135**(44): p. 16438-45.
143. Lee, S.Y., et al., *Biophysical and chemical handles to control the size of DNA nanoparticles produced by rolling circle amplification.* Biomater Sci, 2016. **4**(9): p. 1314-7.
144. Kim, K.-R., et al., *Shaping Rolling Circle Amplification Products into DNA Nanoparticles by Incorporation of Modified Nucleotides and Their Application to In Vitro and In Vivo Delivery of a Photosensitizer.* 2018. **23**(7): p. 1833.
145. Wu, W., et al., *An aptamer-based biosensor for colorimetric detection of Escherichia coli O157:H7.* PLoS One, 2012. **7**(11): p. e48999.
146. Jiang, Y., et al., *Developing a dual-RCA microfluidic platform for sensitive E. coli O157: H7 whole-cell detections.* 2020. **1127**: p. 79-88.
147. Chen, J., et al., *Enzyme-free synthesis of cyclic single-stranded DNA constructs containing a single triazole, amide or phosphoramidate backbone linkage and their use as templates for rolling circle amplification and nanoflower formation.* Chem Sci, 2018. **9**(42): p. 8110-8120.
148. Jiang, H., et al., *Ultrasensitive, label-free detection of T4 ligase and T4 polynucleotide kinase based on target-triggered hyper-branched rolling circle amplification.* 2018. **260**: p. 70-77.
149. Mizutani, A. and M. Tanaka, *Direct and quantitative electrophoretic detection of covalently closed DNA circles formed by in vitro ligation.* Analytical Biochemistry, 2018. **553**: p. 54-56.
150. Joffroy, B., et al., *Rolling circle amplification shows a sinusoidal template length-dependent amplification bias.* Nucleic Acids Res, 2018. **46**(2): p. 538-545.

151. Mao, Y., et al., *Optimal DNA templates for rolling circle amplification revealed by in vitro selection.* Chemistry, 2015. **21**(22): p. 8069-74.
152. Kuhn, H., V.V. Demidov, and M.D.J.N.a.r. Frank-Kamenetskii, *Rolling-circle amplification under topological constraints.* 2002. **30**(2): p. 574-580.
153. Shimada, M., S. Inouye, and M. Inouye, *Requirements of the secondary structures in the primary transcript for multicopy single-stranded DNA synthesis by reverse transcriptase from bacterial retron-Ec107.* Journal of Biological Chemistry, 1994. **269**(20): p. 14553-14558.
154. Sharp, P.A., B. Sugden, and J.J.B. Sambrook, *Detection of two restriction endonuclease activities in Haemophilus parainfluenzae using analytical agarose-ethidium bromide electrophoresis.* 1973. **12**(16): p. 3055-3063.
155. Karapetian, A.T., et al., *Theoretical treatment of melting of complexes of DNA with ligands having several types of binding sites on helical and single-stranded DNA.* 1996. **14**(2): p. 275-283.
156. Vogel, B. and S. Frantz, *Determination of DNase activity by degradation of ethidium bromide-DNA complexes using a fluorescence plate reader.* Anal Biochem, 2015. **471**: p. 73-9.
157. Liu, M., et al., *Target-Induced and Equipment-Free DNA Amplification with a Simple Paper Device.* Angew Chem Int Ed Engl, 2016. **55**(8): p. 2709-13.
158. Wang, L., et al., *Engineering Micrometer-Sized DNA Tracks for High-Speed DNA Synthesis and Biosensing.* 2020. **132**(51): p. 23147-23151.

# Appendix

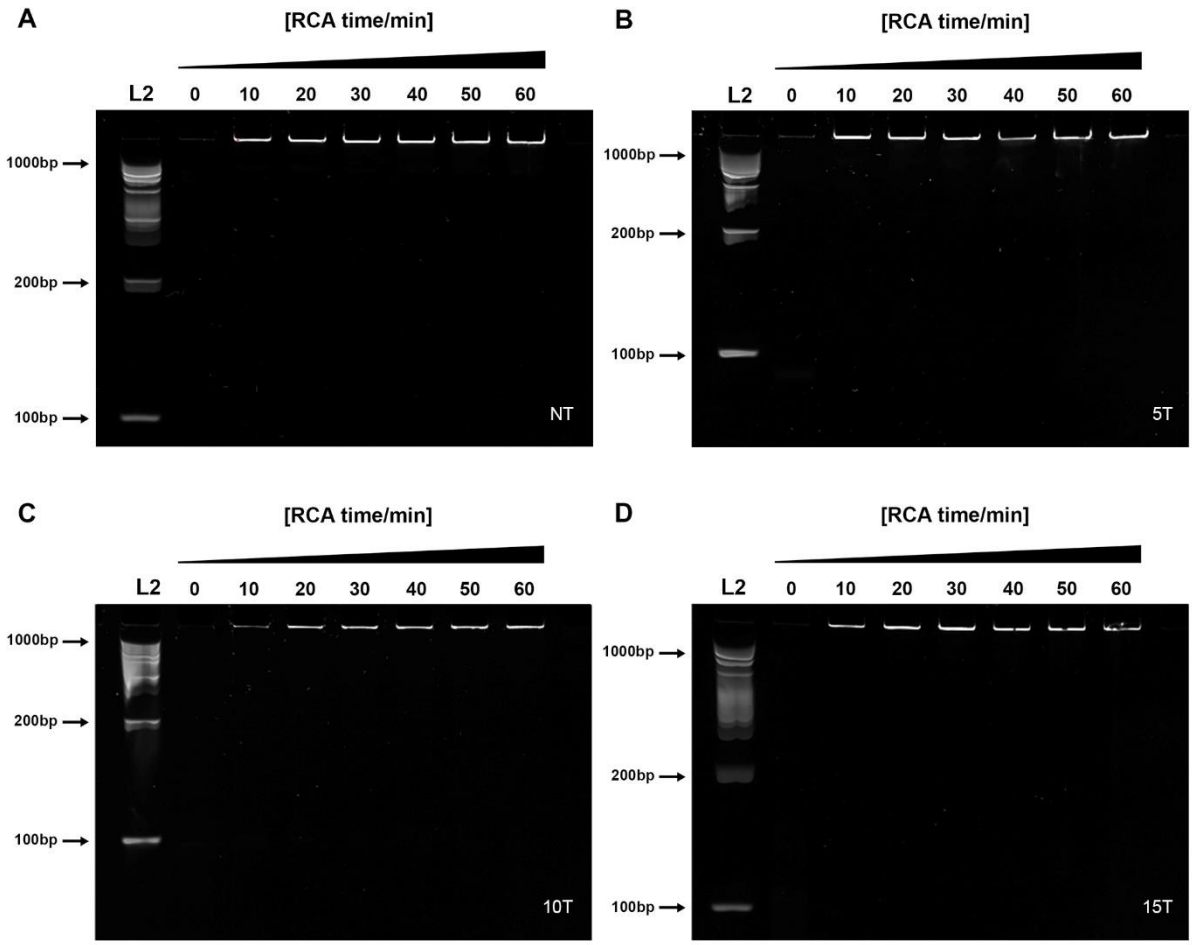


Figure S 1. SYBR Gold-stained RCAP. RCAP was generated by different templates using (A) NT, (B) 5T, (C) 10T, and (D) 15T. In each figure, Lane 1 shows the DNA marker. The rest of lanes are the RCAPs terminated from 0 to 60 min. The RCA reaction was stopped by inactivating phi29 at 65°C for 10 min. The resultant products were resolved by 8% native PAGE, as mentioned in Section 4.3.

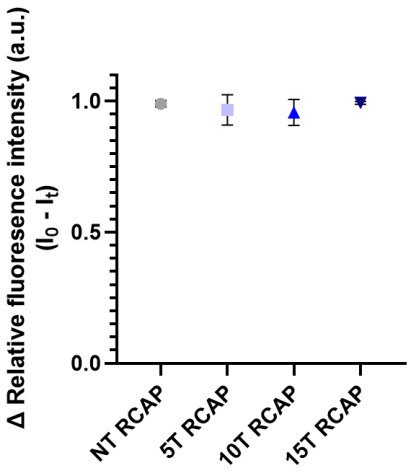


Figure S 2. A plot of changes in relative fluorescence intensity (Δ relative fluorescence intensity) against reaction times. Assuming one unit in Δ relative fluorescence intensity change represents the complete up-shifting of a fixed number of free Cy3-probes. (the number of circular probe template : Cy3-probe= 1: 100). The experiment was conducted with technical triplex. Error bars represent the standard deviations (n = 3).

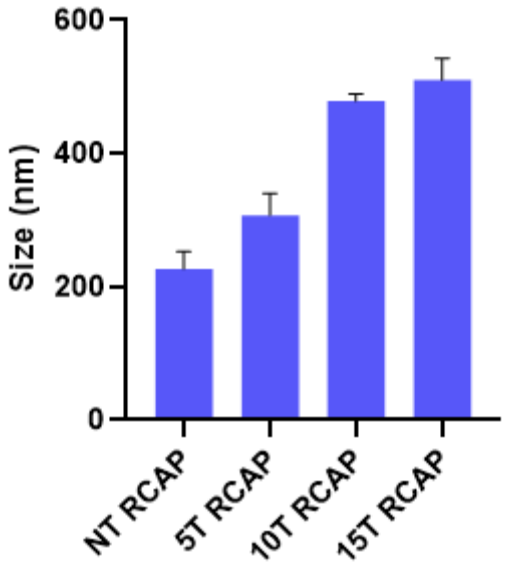


Figure S 3. DLS analysis showing hydrodynamic sizes of pure RCAP generated by NT, 5T, 10T and 15T template. Error bars represent the standard deviations (n = 3).